1 **Effects of frontal area density on outdoor thermal comfort and air**

2 **quality**

3 Zhengtong Li [a], Hao Zhang [a], Chih-Yung Wen [a], An-Shik Yang [b,*], Yu-Hsuan Juan [b]

4 [a] Department of Mechanical Engineering and Interdisciplinary Division of Aeronautical and Aviation Engineering, The Hong Kong Polytechnic University,
5 Kowloon, Hong Kong
6 [b] Department of Energy and Refrigerating Air-Conditioning Engineering, National Taipei University of Technology, Taipei 106, Taiwan, ROC

7 * corresponding author

8

9 **Abstract:**

10 This paper systematically investigates the effects of the frontal area density of various

11 three-dimensional (3D) array building models on the thermal comfort and air quality at

12 the pedestrian level above four sidewalks (north, south, east and west). The buoyancy

13 force for natural-convection flows and the realistic solar irradiance at local solar times

14 (LSTs) from 0700 to 1700 are considered with five different frontal area densities (λ_F

15 = 0.0825–1.25). By a combination of the Rayman model and the ANSYS Fluent®

16 software, the CO concentration and physiologically equivalent temperature (PET) are

17 solved numerically. The simulated CO concentration and PET results are considered as

18 outdoor parameters of the air quality and thermal comfort. A critical λ_F is obtained for

19 urban development by applying multivariable regression analysis to a group of

20 dimensionless parameters. This analysis will facilitate the choice of building density

21 and simultaneously enhance the air quality and thermal comfort. The results reveal that

22 with an increase in λ_F, the PET decreases above most of sidewalks during the daytime,

23 while only is a steady reduction of air quality observed above west and east sidewalks

24 of spanwise streets. According to the multivariable regression analysis for Hong Kong,

25 the building density should have a λ_F value between 0.82 and 0.84 to basically realize

26 a PET < 38 °C and CO concentration < 30000 $\mu g/m^3$ simultaneously in the daytime in

27 June.

28 **Keywords:** Frontal area density; outdoor thermal comfort; air quality; realistic solar

29 radiation; computational fluid dynamics

30

1 **Nomenclature**

h_c	Heat transfer coefficients [W/(m2•K)]
u_i	Velocity component in the i axis
z_0	Roughness length, [m]
AQ	Air quality
AT	Air temperature [℃]
C	Pollutant concentration [mg/m^3]
$C*$	Normalized pollutant concentration
D	Molecular diffusion coefficients
D_t	($= v_t/S_{ct}$) turbulent diffusion coefficients
H	Building height [m]
H/W	Street aspect ratio
L_P	Length of pollutant source [m]
LST	Local solar time
PET	Physiologically equivalent temperature [℃]
TC	Thermal comfort
U_{ABL}	Neutral ABL (Atmospheric boundary layer) velocity [m/s]
U_{ref}	Reference wind speed [m/s]
W	Street width [m]
W_P	Width of pollutant source [m]
WV	Wind velocity [m/s]
SVF	Sky view factor
Sp-$canyon$	Spanwise street canyon
St-$canyon$	Streamwise street canyon
T_{ref}	Reference temperature [℃]
β	Thermal expansion coefficient
λ_F	($= A_F$ (frontal area) $/ A_T$ (total surface area)) Frontal area density
ρ_{ref}	Reference density [kg/m^3]
u^*_{ABL}	ABL friction velocity [m/s]

2

3 **1. Introduction**

4   Due to increasingly severe climate change and harsh heat waves with ongoing

5 urbanization, the resulting high air temperature has been proved to have adverse effects

6 on human morbidity and mortality [1, 2]. Accordingly, outdoor thermal comfort is a

7 growing health concern, especially in densely built areas [2, 3]. On the other hand,

8 traffic emissions, as significant sources of air pollution in urban areas, have also

1 increased sharply[4], revealing the further deterioration of the air quality within the

2 urban canopy layer [5]. Air quality also becomes a critical societal issue because of its

3 detrimental consequences to the health of residents [6]. In summary, urban planners

4 must soon formulate a guideline for alleviating these two severe urban problems

5 simultaneously.

6   In conjunction with full-scale field measurements and wind tunnel experiments,

7 the application of computational fluid dynamics (CFD) simulation to the urban

8 environment has been endorsed as a powerful tool to cover a range of topics involving

9 thermal comfort and air quality [7–12]. Table 1 provides an overview (20 papers) of

10 the studies on thermal comfort and air quality by the CFD technique, listed in

11 chronological order. Even if not all of the studies related to thermal comfort and air

12 quality are included in this table, it tries to summarize the types of urban configuration,

13 the main impact factors, the evaluation parameters, the methods and test data for

14 validation, and the turbulence modeling approaches. The following general conclusions

15 can be made:

16   First, as summarized in Table 1, 4 major factors of the thermal comfort and air

17 quality have been studied in the literature: a) urban geometries (aspect ratio [13–17],

18 frontal area density [18], plan area density [14,19], deviation of building height [18],

19 urban skyline configuration [20], building elevation[21], etc.); b) bulk Richardson

20 number, consisting of ambient wind parameters (wind velocity [15,18,22] and direction

21 [24,25]), and the distribution and strength of surface thermal fluxes (thermal

22 stratifications [26], solar position [23,25,27,28] and temperature difference between the

23 wall and air [15,16]); c) thermal properties of building materials [29,30]; and d) urban

24 greening modifications, such as vegetation cover [17,31]. Among these four factors,

25 only building geometries and the bulk Richardson number are directly related to the

26 thermal comfort and air quality simultaneously. From an urban planner standpoint,

27 urban geometry tends to be a more controllable factor in pursuit of a better outdoor

28 environment. Addititonally, the impacts of some urban geometries on the thermal

comfort and air quality are opposite in trend based on the results mentioned above. Specifically, lower urban densities enhance the removal of pollutants [18,19], but a better thermal comfort state occurs at higher urban densities [25].

Usually, the urban density can be classified by its frontal area density, λ_F (defined as the ratio of the frontal area, A_F, to the total surface area, A_T; see Fig. 2(b)), or plan area density, λ_P (defined as the ratio of the plan area, A_P, to the total surface area, A_T). However, utilization of the frontal area density to represent the building arrays in the most densely populated cities is more practical, as numerous high-rise buildings that cause height blockages can be found in urban areas such as Hong Kong, Singapore, and New York [32]. Based on previous literature, the typical frontal area density of Hong Kong ranges from 0.4 [33] to 1.07 [34]. Accordingly, the frontal density area will be chosen to study its influence on pollutant concentration and thermal comfort in the first place. The objective is to find out the critical frontal area density for the improvement of the outdoor thermal environment with reduced outdoor air pollution at the same time.

Second, the literatures in Table 1 were mainly based on the hypothesis of uniform wall temperature. Only a few dealt with the non-uniform wall temperature caused by the realistic solar heating. Nazarian et al. [28] emphasized the importance of realistic non-uniform thermal forces within 3D building arrays. This non-uniform distribution of surface temperatures could lead to different flow patterns, as opposed to the cases of uniform thermal forcing in 2D street canyons. Similarly, Chen et al. [35] revealed that only in some specific conditions, the uniform wall temperature condition could yield similar results of the realistic non-uniform wall temperature condition. Hence, it is not suggested to define the thermal wall conditions as a uniform wall temperature for the simulation of urban thermal environment[28]. On the other hand, among those studies performed with 3D models, most simulated the buoyancy force in full-scale models to achieve the realistic Richardson number [17,25,27–31]. Hence, this leads to the authors' attempt to account for the realistic solar heating model in the present simulations.

Lastly, some parameters used to evaluate the outdoor thermal comfort and air quality are summarized. Previous studies implemented the air temperature [27], predicted mean vote[24], physiologically equivalent temperature [17,30,31], and standard effective temperature [25] as the criteria for judging the outdoor thermal comfort. In addition, the wind velocity [29] or velocity ratio [5,24], pollutant concentration[13,16,23], air exchange rate [15,20,22,28,36,37], local mean age of air[14,19], pollutant retention time [20], purging flow rate [18], personal intake fraction[38,39] have been used to evaluate the capacity of outdoor ventilation and pollutant dilution. In present study, the PET and carbon monoxide (CO) concentration will be chosen for the evaluation of outdoor environment.

It is noteworthy that there are few studies on urban geometry that address the increasingly severe issues of thermal comfort and air quality simultaneously. Only Zhang et al. [24] examined these two problems at the same time, but they mainly focused on probing the effect of a new building on its surrounding environment under a constant air temperature. Solar radiation was not incorporated into their analysis. Therefore, the impact of urban geometry, especially the frontal area density of urban arrays, on thermal comfort and air quality with consideration of a realistic thermal effect remains poorly understood and is worth investigating.

The aims of this study are to (1) explore the flow behavior, distribution of the air temperature, and pollutant dispersion in full-scale ideal urban arrays with varied frontal area densities; (2) further process the thermal comfort and air quality by using a multivariable regression analysis; and (3) finally compare the indicators of thermal comfort and air quality at the pedestrian level to propose a critical frontal area density for improving the outdoor thermal comfort and air quality simultaneously.

In section 2, the methodological framework is established. This paper presents the simulation details of the CFD setup, including the model description, boundary condition, numerical method, and grid independence. In addition, the Rayman model is explained, including its coupling with the CFD model, the computation of the sky view

factor (SVF), and the input of personal data. Finally, the evaluation parameters, including the CO concentration and PET, are introduced. In section 3, we validate the present computational model with the turbulence modeling tested. The influences of the frontal area density on the air temperature, wind velocity, PET, and pollutant concentration are elucidated. Based on multivariable regression analysis of the pollutant concentration and PET, a better balance is sought between thermal comfort and air quality. In section 4, a discussion on the limitations of this study and suggestions for urban planners are presented. Finally, the conclusions are given in section 5.

Table 1 Overview of CFD studies on urban microclimate problems (AQ and TC) in the built environment

Study	Ref.	Buoyancy force	Focus	Sensitivity analysis	Urban configuration	Evaluation parameter	Validation	Turbulence model
Xie et al. (2007)	[13]	Yes	AQ	a	RS/2D/Generic/Street canyon	PC	AT, WV (WT)	Steady RANS (RNG)
Xie et al. (2006)	[22]	Yes	AQ	b	RS/2D/Generic/Street canyon	AER	AT, WV (WT)	Steady RANS (SKE, RNG, RKE)
Buccolieri et al. (2010)	[19]	No	AQ	a	RS/3D/Generic/Building arrays	Age	-	Steady RANS (SKE)
Zhang et al. (2011)	[24]	Yes	AQ/TC	b	FS/3D/Realistic/City part	PMV/VR	C_p (WT)	Steady RANS (SKE)
Hang et al. (2012)	[18]	No	AQ	b	RS/3D/Generic/Building arrays	PFR	WV, TKE (WT)	Steady RANS (SKE, RNG)
Qu et al. (2012)	[29]	Yes	AQ	c	RS/3D/Generic/Building arrays	WV	-	Steady RANS (-)
Santiago et al. (2014)	[27]	Yes	TC	b	RS/3D/Generic/Building arrays	AT	AT, WV (WT)	Steady RANS (-)
Ramponi et al. (2015)	[14]	No	AQ	a	FS/3D/Generic/Building arrays	Age	C_p (WT)	Steady RANS (SKE)
Tan et al. (2015)	[23]	Yes	AQ	b	FS/2D/Generic/Street canyon	P C	ST (FM)/ AT, WV (WT)	Steady RANS (RNG)
Nazarian and Kleissl (2016)	[28]	Yes	AQ	b	FS/3D/Generic/Building arrays	AER	WV, ST (WT1) /AT (WT2)	LES
Liu et al. (2016)	[21]	Yes	TC	a	FS/3D/Generic/Building arrays	PET	WV (WT)	Steady RANS (RNG)/ DDES
Mei et al. (2016)	[15]	Yes	AQ	a, b	RS/2D/Generic/Street canyon	AER	AT, WV (WT)	Steady RANS (RKE)
Lin et al. (2016)	[16]	Yes	AQ	a, b	RS/2D/Generic/Street canyon	PC	WV, TKE (WT1)/ PC (WT2)	Steady RANS (RNG)
Nazarian et al. (2017)	[25]	Yes	TC	a, b	FS/3D/Generic/Building arrays	SET	-	LES
Yang et al. (2017)	[31]	Yes	TC	d	FS/3D/Realistic/City part	PET	WV, WD, AT (FM)	Steady RANS (RKE)
Juan et al. (2017)	[36]	No	AQ	a	RS/3D/Generic/Building arrays	AER	WV, TKE (WT)	Steady RANS (SKE)
Sun et al. (2017)	[17]	Yes	TC	d	FS/3D/Realistic/City part	PET	AT, RH (FM)	-
Wang and Ng (2018)	[26]	Yes	AQ	b	FS/3D/Realistic/City part	VR	WV (WT, FM)	LES
Taleghani et al. (2018)	[30]	Yes	TC	c	FS/3D/Realistic/City part	PET	-	-
Mei et al. (2019)	[20]	Yes	AQ	a	FS/2D/Generic/Street canyon	AT/AER/PRT/PC	WV, AT (TR)	Unsteady RANS (SST)

AER = Air exchange rate, Age = Local mean age of air, AQ = Air quality, AT = Air temperature, C_p = Pressure coefficient, DDES= Delayed Detached Eddy Simulation, FM = Field measurement, FS = Full scale, FP = Flow patterns, LES = Large eddy simulation, Nu = Nusselt number, PC = Pollutant concentration, PET = Physiologically equivalent temperature, PFR = purging flow rate, PMV = Predicted mean vote, PRT = Pollutant retention time, RANS = Reynolds-averaged Navier-Stokes, R_b = Bulk Richardson number, RH = Relative humidity, RKE = Realizable k-ε model, RNG =

2. Methodology

2.1 Methodological framework

The present study is devoted to numerically investigating the effect of the frontal area density (λ_F) on the thermal comfort and air quality at the pedestrian level above sidewalks using the commercial software ANSYS Fluent[®]. Figure 1 illustrates the methodological framework of the CFD simulations. First, the necessary ambient parameters and boundary conditions of the ground surfaces and building walls were specified in ANSYS Fluent[®]. In addition, we selected five ideal urban configurations as the input to ANSYS Fluent[®] and SkyHelios to estimate the microclimate data and SVF, respectively. The PET values could be obtained by employing the Rayman 1.2 model with the known microclimate data and SVF. Meanwhile, the pollutant concentration was calculated by Fluent[®] to evaluate the air quality. Finally, for different λ_F settings, the indices of the thermal comfort and air quality were further processed with multivariable regression analysis. A critical λ_F that enhances the thermal comfort and air quality concurrently at the pedestrian level above sidewalks are proposed accordingly.
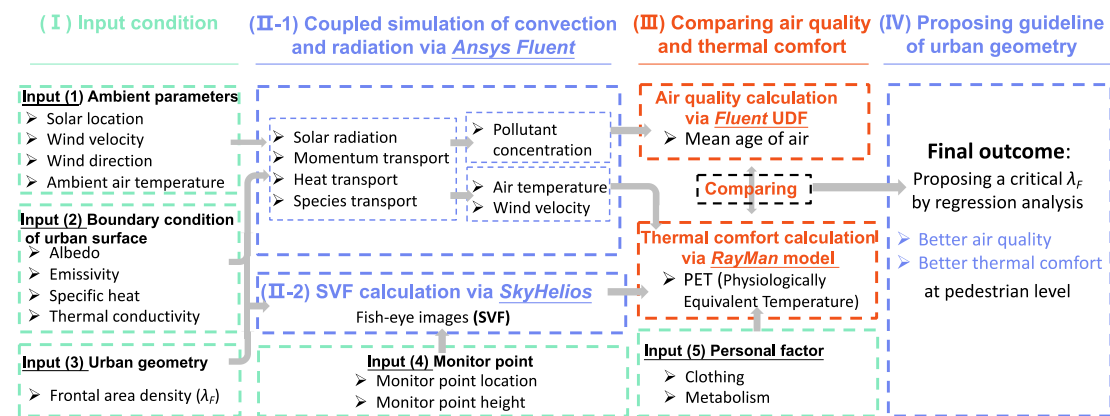

Fig. 1 Methodological framework of simulation.

2.2 CFD numerical model

2.2.1 Model description and simulation setup

The urban geometry under consideration is a 6×6 matrix of buildings with various frontal area densities λ_F (= 0.0825, 0.125, 0.25, 0.75 and 1.25), as shown in Figs. 2(a) and 2(b). As mentioned earlier, λ_F is the ratio of the frontal area (A_F) to the total surface area (A_T). For various H (building height) at a fixed W (street width) of 20 m, the corresponding aspect ratios, H/W, for the above λ_F are 0.33, 0.5, 1, 3 and 5, respectively. Apart from the effect of various λ_F, the calculations were conducted under steady-state weather conditions at a Local Solar Time (LST) between 7 and 17 on a clear summer day (June 15) in Hong Kong.

As depicted in Figs. 2(a) and 2(c), the space among building arrays is separated into two kinds of street canyons, namely, the streamwise street canyon (St-canyon) and the spanwise street canyon (Sp-canyon) because the street orientation can result in different thermal comfort outcomes (this will be discussed later) [40]. In addition, this study adopts the space amid the central four buildings to replicate the scenario of any single building surrounded by many other buildings in Hong Kong. Since the distributions of the air temperature and wind velocity can vary significantly on different sidewalks due to the shadow effect, ten monitoring points on each sidewalk were chosen to examine the associated thermal comfort and air quality at the pedestrian level, as shown in Fig. 2(c). These points are arranged 1 m away from the building's surface and 1.5 m aboveground (the pedestrian height). According to the practice guidelines given by Tominaga et al. [41], the dimensions of the computational domain are based on the parameter H as follows: the axial distance between the velocity inlet and windward faces of the first row of buildings is 5H, the spanwise ranges between the sidewalls of buildings and symmetric boundaries on both sides are all 5H, and the outlet boundary is 15H away from the leeward faces of the last row of buildings, as displayed in Fig. 2(a).

1   The theoretical model, formulated in the ANSYS/Fluent® CFD software (Release

2   15.0), was used to simulate the flow of ambient wind over ideal urban street canyons

3   under the effect of realistic solar heating to evaluate the thermal comfort and air quality

4   at the pedestrian level. According to the observation data from the Hong Kong

5   Observatory Weather Station (longitude: 22°18'07" N, latitude: 114°10'27" E and

6   elevation of ground above mean sea level: 32 m)[42], the hourly means of

7   meteorological data in June in Hong Kong (for 20 years) were obtained (air temperature,

8   relative humidity, prevailing wind direction, and wind speed) for the inlet boundary

9   condition. The wind speed occurs most frequently at 3 m/s from the east (90°) at a

10   height of 32 m above sea level. The mean hourly air temperature is summarized in Table

11   A.1. The profiles of the neutral ABL velocity (U_{ABL}), turbulent kinetic energy (k), and

12   turbulence dissipation rate (ε) were resolved as the incoming airflow conditions at the

13   velocity inlet.

14
$$U_{ABL} = \frac{u^*_{ABL}}{K} \ln(\frac{z + z_0}{z_0}),$$
(1)

15
$$k = \frac{(u^*_{ABL})^2}{\sqrt{C_\mu}},$$
(2)

16
$$\varepsilon = \frac{(u^*_{ABL})^3}{K(z + z_0)},$$
(3)

17   where u^*_{ABL} is the ABL friction velocity for the calculation of inlet U_{ABL}, k, and ε, which

18   can be computed from the reference wind velocity $U_{ref} = 3$ m/s at a reference height h

19   (32 m) as follows:

20
$$u^*_{ABL} = \frac{K U_{ref}}{\ln(\frac{h + z_0}{z_0})},$$
(4)

21   where K and z_0 are the von Karman's constant (≈ 0.4) and the aerodynamic roughness,

22   respectively.

1   To model the drag force induced by aerodynamic roughness for wind crossing the

2   terrain surface, this study implemented the standard wall function method utilizing the

3   logarithmic law for the velocity profile, with $z_0= 2$ m prescribed due to the simulation

4   involving the presence of high-rise and concrete-frame mixed-use commercial and

5   residential buildings [43].

6   To accurately resolve the surface temperatures of buildings, the radiative heat

7   fluxes resulting from the significant solar radiation effect need to be computed. With

8   the input of the specific time data and the global location, the accurate position of the

9   sun can be calculated by the Solar Calculator dialog box of ANSYS Fluent®, and its

10   Ray-Tracing model can provide the incident radiation on those exposed surfaces. Thus,

11   the direct solar radiation was added into the energy equation as a source term. In other

12   word, the thermal load resulted from the solar radiation will be applied as a boundary

13   condition. Moreover, this study applied the discrete ordinates (DO) radiation model to

14   evaluate the radiant heat fluxes between the surfaces since it is appropriate to account

15   for the optical problems in a complex-geometry system with a high degree of accuracy

16   [29]. As reported by Dugaria et al.[44], the DO model could yield a close coupling

17   between wall temperature and radiative energy, in which the same mesh is adopted to

18   effectively cope with radiative transfer, energy, mass and momentum conservation

19   problems. Notably, the input values of radiation in the PET calculation will be

20   elaborated in section 2.3. The spectral optical and thermophysical properties of the

21   involved materials are summarized in Table A.2. In addition, the heat transfer

22   coefficients (h_c) of the building faces and ground are calculated by the following

23   empirical correlation [31].

24       $$h_c = 5.7 + 3.8 V_{air},$$ (5)

25   where V_{air} is the airflow velocity.

26   To calculate the pollutant concentration, eight uniform volume sources (width W_p

27   $= 2$ m and length $L_p = 20$ m) were specified near the ground between $z = 0$ m and 0.5 m

1   to represent traffic lanes in opposite directions on two sides of the street canyon, as

2   shown in Fig. 2(d).
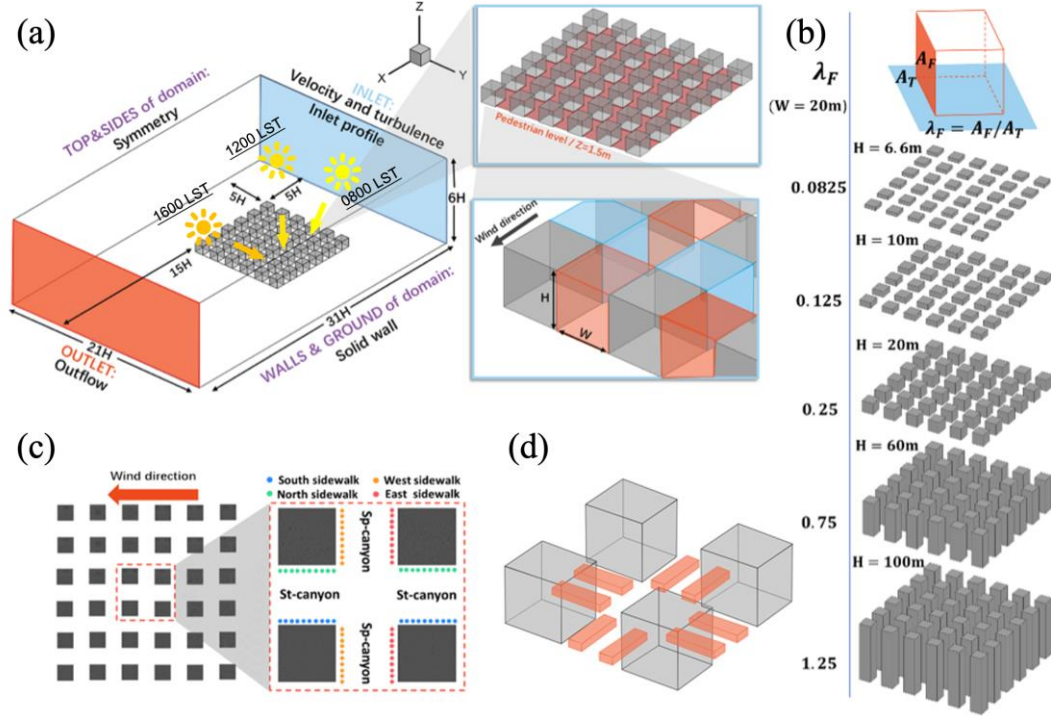
3

4   Fig. 2 (a) Geometric model, boundary conditions, sun positions (0800, 1200, and 1600 LST) and schematic diagrams

5   showing the pedestrian level and spanwise (Sp-canyon, red) and streamwise (St-canyon, blue) street canyons.

6   (b) Schematic diagrams showing the urban-like geometries investigated with increasing λ_F. (c) Schematic

7   diagrams showing the monitoring points for the thermal comfort and air quality. (d) Schematic diagrams

8   showing the volumetric pollutant sources.

9   **2.2.2 Governing equation and turbulence model**

10   The numerical analysis was based on the steady-state 3D RANS conservation

11   equations of mass, momentum, and energy for the incompressible turbulent flow. The

12   governing equations are given below:

13   Continuity equation:

14       $$\frac{\partial u_i}{\partial x_i} = 0, \tag{6}$$

15   Momentum equation:

1
$$\frac{\partial \rho u_i u_j}{\partial x_j} = -\frac{\partial p}{\partial x_i} + \frac{\partial}{\partial x_j}\left[(\mu+\mu_t)\left(\frac{\partial u_i}{\partial x_j}+\frac{\partial u_j}{\partial x_i}\right)\right] + \rho_{ref}\, g_i \beta\left(T-T_{ref}\right),$$
(7)

2   Energy equation:

3
$$\frac{\partial u_i T}{\partial x_i} + \frac{\partial}{\partial x_i}(\alpha_T\frac{\partial T}{\partial x_i}) = Q_T,$$
(8)

4   where u_i denotes the air velocity component along the i axis; p, ρ, T, μ, μ_t, g_i, and α_T

5   represent the pressure, density, temperature, dynamic viscosity, turbulent viscosity,

6   gravity acceleration, and thermal diffusivity, respectively. Q_T represents the heat flux

7   caused by solar radiation. To model the buoyancy-driven flow, the Boussinesq

8   approximation was adopted in the numerical model, $\rho = \rho_{ref}\beta(T\text{-}T_{ref})$ in Eq. (7), where

9   β, T_{ref}, and ρ_{ref} are the thermal expansion coefficient, reference temperature, and

10   reference density, respectively. In the current study, the air density was treated as a

11   constant value in all equations, except for the buoyancy term in the momentum equation.

12   In addition, the species transport equation was solved to probe the pollutant dispersion

13   in an urban environment as follows:

14
$$\frac{\partial u_i Y}{\partial x_i} - \frac{\partial}{\partial x_i}\left[(D+D_t)\frac{\partial Y}{\partial x_i}\right] = S,$$
(9)

15   where D and D_t ($= v_t/S_{ct}$) denote the molecular and turbulent diffusion coefficients of

16   pollutants. Here, v_t is the turbulent viscosity, and S_{ct} is the turbulent Schmidt number,

17   which is set as 0.4 to account for the underestimation of the turbulent mass diffusion

18   from the RANS models [45]. Y is the mass fraction of the pollutant distribution. Herein,

19   we selected CO as a tracer gas, and S is the source term for CO. The constant emission

20   rate per hour and unit street length (36.1 g/h/m, i.e., total mass release rate of $L_p \times 1.0$

21    $\times 10^{-5}$ kg/s) is adopted for each CO source with reference to Ng and Chau [6].

22   Considering the type and number of vehicles passing by a realistic street per hour in

23   Mongkok, Hong Kong, Ng and Chau [6] calculated the pollutant release rate above.

24   As mentioned in Table 1, the steady RANS approach is most commonly used to

25   simulate buoyant airflows, with successful validation results achieved between these

26   predictions and the measured data. In addition, the steady RANS model could be used

27   to solve the intricate mechanically driven and thermally driven flow processes in a more

1 time-efficient way. Thus, this work applied the steady RANS turbulence model to

2 evaluate the wind and thermal environments as well as the pollutant dispersion within

3 the urban arrays. The simulation sensitivity check by different turbulence models

4 (standard, RNG, and realizable k-ε model) was also performed against the wind tunnel

5 experimental data. According to the validation study in section 3.1, the RNG k-ε model

6 is most suitable for the present study to provide reliable predictions of the mean flows

7 with the thermal effect and pollutant dispersion. The RNG k-ε model, developed by

8 Yakhot and Orszag [46], can simulate a wide range of turbulent flow phenomena to

9 effectively characterize the airflow and pollutant transport in street canyons under the

10 thermal buoyancy force effects [13,22]. The conservation equations of the RNG k-ε

11 turbulence model for the turbulence kinetic energy (k) and dissipation rate (ε) are as

12 follows:

13
$$\frac{\partial \rho k u_i}{\partial x_i} = \frac{\partial}{\partial x_i}\left[(\mu + \frac{\mu_t}{\sigma_k})\frac{\partial k}{\partial x_i}\right] + P_k + G_b - \varepsilon , \tag{10}$$

14
$$\frac{\partial \rho \varepsilon u_i}{\partial x_i} = \frac{\partial}{\partial x_i}\left[(\mu + \frac{\mu_t}{\sigma_\varepsilon})\frac{\partial k}{\partial x_i}\right] + C_{\varepsilon 1}\frac{\varepsilon}{k}(P_k + C_{\varepsilon 3}G_b) - C_{\varepsilon 2}\frac{\varepsilon^2}{k} , \tag{11}$$

15 where the production terms of the turbulent kinetic energy due to buoyancy (G_b) and shear

16 (P_k) can be expressed as follows:

17
$$G_b = \beta \frac{\mu_t}{\mathrm{Pr}_t}\frac{\partial T}{\partial x_i} g_i , \tag{12}$$

18
$$P_k = \nu_t (\frac{\partial u_i}{\partial x_j} + \frac{\partial u_j}{\partial x_i})\frac{\partial u_i}{\partial x_j} . \tag{13}$$

19 Here, $\mu_t = C_\mu \rho k^2/\varepsilon$. The constants C_μ, σ_k, σ_ε, $C_{\varepsilon 1}$, and $C_{\varepsilon 2}$ are 0.0845, 0.7194, 0.7194, 1.42

20 and 1.68, respectively. The factor $C_{\varepsilon 3} = \tanh\left|\frac{v}{u}\right|$, where v and u are the velocity

21 components of the flow parallel and perpendicular to the gravitational vector,

22 respectively.

1 **2.2.3 Numerical method**

2   The aforementioned governing equations were discretized by the finite volume

3 scheme in ANSYS Fluent®. This study utilized the pressure-linked equations consistent

4 (SIMPLEC) numerical method for pressure-velocity coupling. The second-order

5 upwind scheme was adopted to discretize both the convective terms and diffusion terms.

6 A double-precision solver was also selected for CFD calculations. The convergence of

7 the normalized residual errors of the energy equation was set to 10^{-9}, whereas the

8 convergence criterion of the remaining equations was set to 10^{-6}.

9 **2.2.4 Mesh description and mesh-independent validation**

10   ANSYS ICEM® was employed as a preprocessor to construct computational grids

11 for our numerical models. Herein, this study implemented fully structured hexahedral

12 (HEX) cells to ensure the high quality of the computational mesh system. With

13 consideration of the relatively large temperature and pollutant concentration gradients

14 near the ground and building surfaces, the finest grids were arranged around these two

15 kinds of walls, with a grid expansion ratio of 1.05 employed in the bigeometric mesh

16 law in street canyons.

17   To conduct the mesh-independent study, the case of $\lambda_F = 0.25$ is referred to as the

18 base model, with three different grid densities under the same environmental conditions

19 (LST = 8, U_{ref} = 3 m/s). For coarse/medium/fine meshes (with cell numbers of

20 3,569,046, 6,625,578, and 9,778,068, respectively), finest grid sizes of 1/0.5/0.25 m

21 were set directly above the ground and building surfaces, and at least 10/20/25 grids

22 were disposed in all directions within a street canyon. For all three meshes, the

23 streamwise grid size increased from the first row of building arrays to the inlet and from

24 the last row to outlet, with a ratio of 1.05 and 1.2, respectively. Figure 3(a) compares

25 the predicted wind velocity and air temperature of the three calculation cases on the

26 west (Sp-canyon) and north (St-canyon) sidewalks (average value of 10 monitoring

27 points at each sidewalk) in Fig. 2(c). The differences in the computed wind velocity on

1   the north and west sidewalks were 8.3% and 9.5% between the coarse grids and medium

2   grids, respectively. Alternatively, the corresponding discrepancies of the predictions on

3   the north and west sidewalks were reduced to 1.5% and 2.3%, respectively, between

4   the medium grids and fine grids. Although only 3.2% and 1.7% deviations in the air

5   temperature occurred between the coarse grids and medium grids, respectively, the

6   differences in the computed air temperature were further reduced to 0.7% and 0.8%

7   between the medium grids and fine grids, respectively. Due to intricate physical

8   problems involved (short-wave solar irradiation, long-wave radiation amongst building

9   surfaces, and pollutant dispersion), almost 61h of central processing unit (CPU) time is

10   required to reach a converged steady-state solution on an Intel Core® X900-3.47 GHz

11   (128 GB RAM) high-performance workstation. Notably, the average $y+$ of the building

12   surfaces and grounds are 1038.6 for the medium mesh, which is slightly higher than the

13   upper bound of $y+$ (500) for standard wall function recommended by An et al.[47].

14   Although $y+$ of the fine mesh (519.3) could basically reach the requirement of $y+$,

15   nearly 12h extra processing time is need for the convergence. As reported by An et

16   al.[47], a suitable relaxation of the restriction in $y+$ value should be allowed, with a

17   compromise made amongst the prediction accuracy, the numerical stability, and the

18   computational time. Consequently, the medium grid (with a total cell number of

19   6,625,578), as shown in Fig. 3(b), was considered reliable and adopted to perform the

20   numerical analysis. Notably, the grid independence tests of other cases with various

21   urban geometries were also conducted in the same manner before performing the
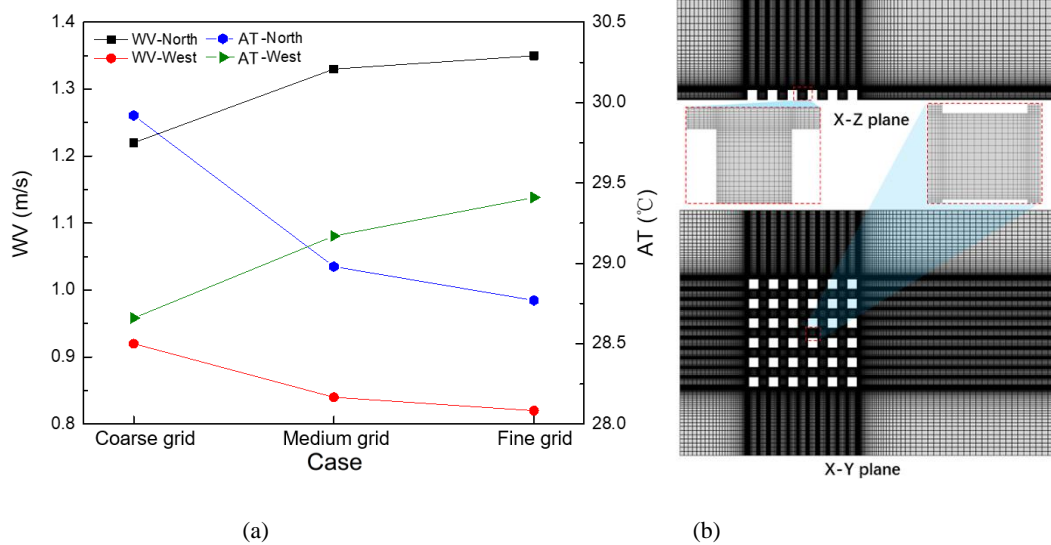
22   numerical analysis.

Fig. 3 (a) Grid-independent validation. (b) Grid distributions of the geometric model: $\lambda_F = 0.25$ / medium grid.(North and West denote the north and west sidewalks.)

2.3 Rayman thermal comfort analysis model

The Rayman model (version 1.2) [48] is a recently developed radiation and thermal comfort model. This model has been widely adopted and extensively evaluated for the outdoor thermal comfort in the urban areas[49,50] with good validation [51,52]. The final output of the Rayman model is the assessment of the thermal comfort with the use of indices, such as the PET and SET. To yield these thermal comfort indices, the calculation of mean radiation temperature is essential. In the Rayman model, its calculation is based on the simulation of shortwave and longwave radiation flux densities from the 3D environment, sunshine durations, and shadow spaces experienced by the human-biometeorological reference person [52]. Therefore, one needs to input the time of day, cloud coverage, air temperature, wind velocity, and SVF (from fish-eye images). As mentioned above, the air temperature and wind velocity can be obtained from CFD calculations. Additionally, the SkyHelios model [53] has been used to generate virtual fish-eye images for each observation point via inputting a raster input file at a resolution of 0.5×0.5 m. Because ten observation points were used to characterize one sidewalk (see Fig. 2(c)), 80 virtual fish-eye images in total were

1 needed for the simulation case. Figure 4 shows some representative fish-eye images in

2 the middle of the north sidewalk for different urban arrays. Finally, the thermal indices

3 can be obtained at the pedestrian level after inputting personal data, as listed in Table

4 2.
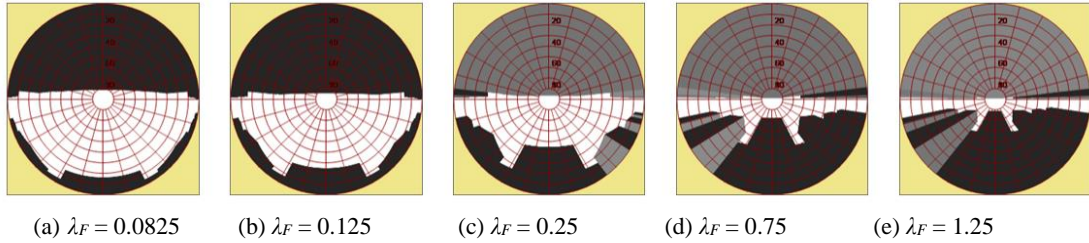
5
6   (a) $\lambda_F = 0.0825$ (b) $\lambda_F = 0.125$ (c) $\lambda_F = 0.25$ (d) $\lambda_F = 0.75$ (e) $\lambda_F = 1.25$
7 Fig. 4 Fish-eye images in the middle of the north sidewalk, obtained from SkyHelios.

8   Table 2 Conditions used in simulations with Rayman 1.2

Position	Hong Kong (22°18' N, 114°10' E)
Simulation time	LST = 8, 12, 16, June 15
Cloud coverage	0 Octa
Humidity (RH)	82%
Activity	80 W (walking)
Clothing	0.5 clo (summer clothes)
Personal data	1.72 m, 65 kg, 30 years, male

9 **2.4 Thermal comfort indices**

10   To facilitate a deeper understanding of the influences of urban geometry and

11 realistic solar radiation on the thermal sensation, the PET is a suitable evaluation index.

12 The PET has been used regularly for the assessment of outdoor thermal comfort [54],

13 considering the impacts of shortwave and longwave radiation fluxes in an outdoor

14 environment on the energy budget of the human body [55]. One of its advantages is that

15 it is a real climatic index describing the thermal environment in a thermal

16 physiologically weighted manner [56]. Second, the PET has a commonly known unit

17 (℃) to measure the thermal stress on outdoor human pedestrians, which could easily

18 be accepted by the public, who are generally not familiar with modern human-bio

19 meteorological terms[57]. The thermal sensation of the PET can be summarized into

20 different "thermal comfort ranges" based on the subjective thermal perception of local

21 people [58,59]. For instance, Lin and Matzarakis [59] conducted a series of studies to

define PET ranges in the hot and humid subtropical context of Taiwan. Due to similar behavioral adjustments of the residents and climatic conditions between Taiwan and Hong Kong, this study introduced the thermal sensation classification in Taiwan (see Table A.3) as a criterion to evaluate the thermal environment above sidewalks.

3. Results

3.1 Validation

To the best of our knowledge, wind tunnel experiments considering both the pollutant dispersion and thermal effect simultaneously are not available. As shown in the studies listed in Table 1, to validate the simulation results of pollutant dispersion, the CFD results were compared with different kinds of wind tunnel data (turbulence kinetic energy [16,18,36], pollutant concentration [16] and pressure coefficient [14,24]), field measurement data (surface temperature[23] and wind velocity [26]), and empirical formulas (air temperature and wind velocity) [20]. On the other hand, to test the validation of thermal effect, wind tunnel data (air temperature and wind velocity) [27] and field measurement data (air temperature [17,31], wind velocity [31], wind direction [31] and relative humidity [17]) were chosen. Accordingly, the thermal measurement data (wind velocity and air temperature) from the wind tunnel experiment by Uehara et al. [60] and the pollutant measurement data (pollutant concentration) from that by Meroney et al. [61] were employed separately to validate the present computational model in CFD simulations.

3.1.1 Validation study of the thermal effect

To validate the thermal effect of the current numerical model, this study referred to the wind tunnel experiment performed by Uehara et al. [60] to investigate the influences of atmospheric stability on airflow over an array of 3D buildings, which has 14 rows of simply shaped blocks with a characteristic height = width = length = 0.1 m for an aspect ratio of 1. In the wind tunnel experiment, the floor panel in the urban areas

1 was heated to a constant ground temperature T_g. To validate the predicted thermal effect,

2 the settings of the CFD simulation were consistent with those of the wind tunnel

3 experiment. Thus, this simulation was performed at a bulk Richardson number (R_b,

4 defined as $gH(T_{in}-T_g/\{(273.15+T_{in})(U_H)^2\})$ of -0.21 (unstable), where T_{in} is the ambient

5 temperature. The measured data in terms of the streamwise wind velocity and air

6 temperature were obtained at the vertical section *(z/H= 0-2)* in the center of the street

7 canyon between the fifth and sixth rows of the building arrays.

8   Figure 5 illustrates a comparison of the simulated vertical profiles of the (a)

9 normalized streamwise velocity *u/U$_{2H}$* and (b) temperature $(T-T_g)/(T_{in}-T_g)$ (by the

10 standard, realizable, and RNG *k-ε* models) with the experimental results from the wind

11 tunnel tests. *u* and U_{2H} are the streamwise velocity and mean wind speed at a height of

12 *2H*, respectively. Clearly, all three turbulence models reasonably predict the streamwise

13 flow velocities in the vortex recirculation region, with some discrepancies occurring at

14 *z/H = 1.25*. Nevertheless, the normalized temperature simulated with the RNG model

15 is in better agreement with that of the wind tunnel experiment than those of the standard

16 and realizable *k-ε* models. The temperature profile predicted by the RNG model near

17 the ground is very close to the wind tunnel data, suggesting good agreement of the sharp

18 near-ground temperature gradient computed using the RNG model. Overall, the RNG

19 *k-ε* turbulence model demonstrates the best prediction capability for the study of

20 thermal effects.
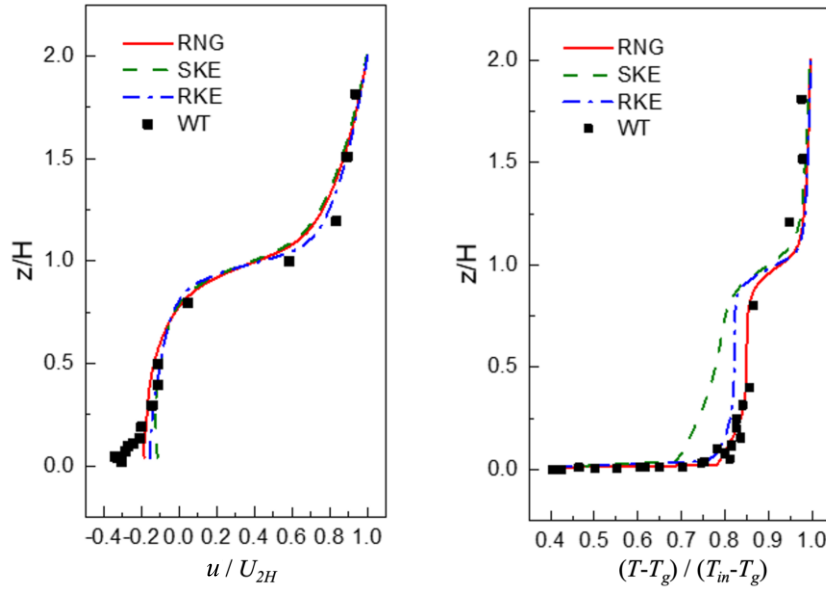
(a) normalized streamwise u/U_{2H} (b) normalized temperature $(T-T_g)/(T_{in}-T_g)$

Fig. 5 Comparison of the simulated data with the wind tunnel data by Uehara et al. [46]. (a) normalized streamwise u/U_{2H} and (b) normalized temperature $(T-T_g)/(T_{in}-T_g)$. SKE, RNG, and RKE denote the standard, RNG, and realized k-ε models, respectively; WT denotes the wind tunnel data.

3.1.2 Validation study of pollutant dispersion

The current computational model for pollutant dispersion simulations was validated against the wind tunnel measurements conducted by Meroney et al. [61], who explored the street geometry effect on the dispersion of traffic pollutants within a 2D street canyon. Two wooden bars with height = width = 0.06 m were mounted across the whole wind tunnel, with the approaching wind direction perpendicular to the canyon axis. A ground-level pollutant line source (ethane, C_2H_6) parallel to the canyon axis was laid in the center of the canyon to represent traffic exhaust. Moreover, the pollutant was continually released at a steady rate of Q_e. The reference wind speed, U_{ref}, was recorded at a reference height of 0.65 m above the floor. To validate the predicted pollutant concentration, the settings of the CFD simulation were consistent with those of the wind tunnel experiment. The predictions of the normalized ethane concentration $C^* = CU_{ref}HL/Q_e$ were compared with the wind tunnel experiment data measured along the leeward and windward walls in the center vertical section of the canyon. Here,

1   C is the volume fraction of ethane, and H and L are the height and the length of the

2   buildings, respectively.

3   As demonstrated in Fig. 6, on the windward side, the standard k-ε turbulence model

4   provides the best-simulated results, whereas the RNG and realizable k-ε turbulence

5   models slightly overestimate the pollutant concentration. On the leeward side, the RNG

6   k-ε turbulence model provides the best-simulated results, although it slightly

7   underpredicts the pollutant concentration in the lower part of the street canyon.

8   Generally, the RNG k-ε turbulence model is the most suitable for predicting the

9   pollutant dispersion and thermal effects with reasonable accuracy simultaneously.
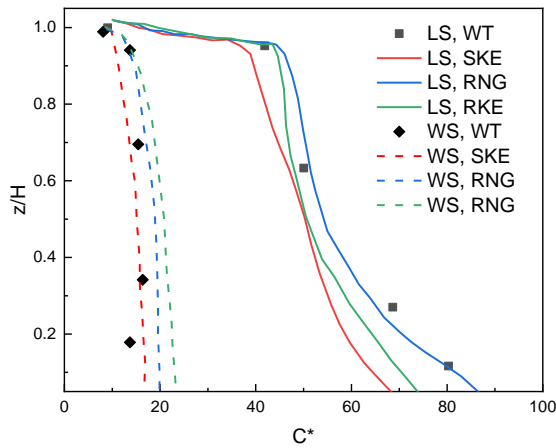
10

11 Fig. 6 Comparison of the simulated data with the wind tunnel data by Meroney et al. [61]. SKE, RNG, and RKE

12   denote the standard, RNG, and realized k-ε models, respectively, WT denotes the wind tunnel data, LS

13   represents the data on the leeward side and WS represents the data on the windward side.

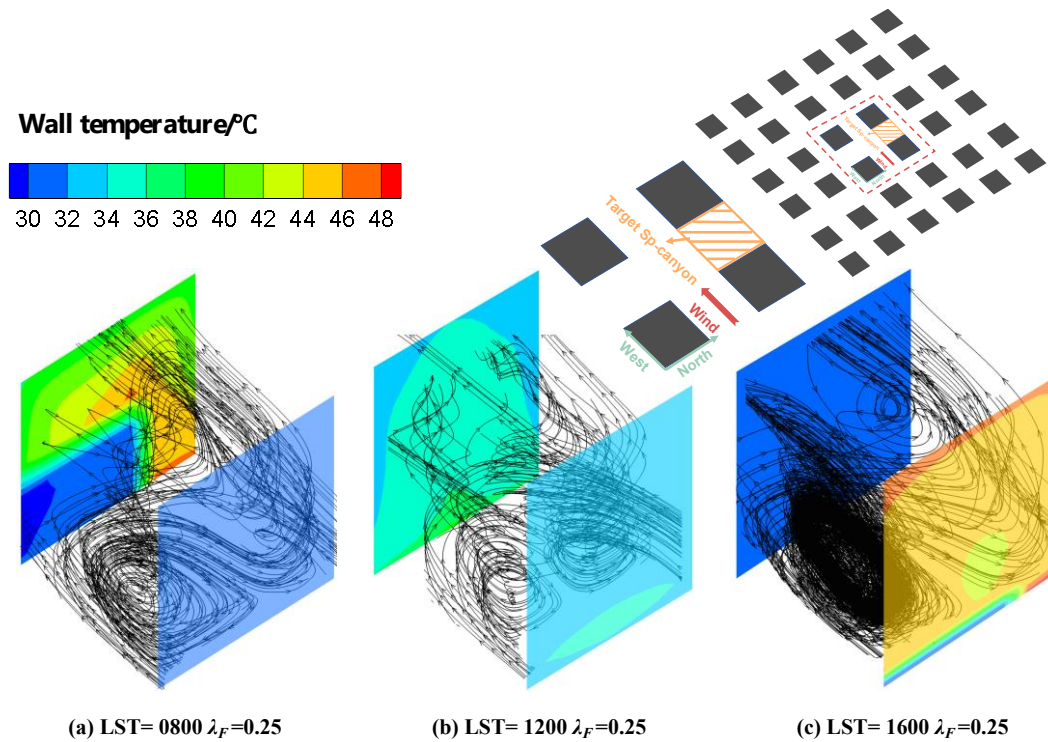14 **3.2 Wind velocity and flow structure**

15   First, the flow structures at various solar times (0800, 1200, and 1600 LST) were

16 tested under $\lambda_F= 0.25$. The surfaces along the St-canyon were almost parallel to the

17 solar irradiation (see Fig. 2(a)), causing a relatively minor change in the wall

18 temperature and consequential flow structure. During the daytime, there were at most

19 0.4 ℃ and 1.7 ℃ changes in the mean surface temperature of south and north walls,

20 respectively. Additionally, the channel flow almost dominated the St-canyon. In

21 contrast, in the Sp-canyon, the related change was more significant. An approximate 20

1 ℃ variation on the surfaces along the Sp-canyon was observed in Fig. 7 and Fig. 8.

2 Accordingly, we probed the distribution of the wall temperature and flow structure in

3 the Sp-canyon.

4 Fig. 7 illustrates the predicted wall temperature and 3D streamlines in the Sp-

5 canyon. The location of these analysis is shown in the inset at the upper right corner.

6 Distinct 3D-flow patterns were observed for these three solar times, attributable to the

7 respective buoyancy-driven mechanisms resulting from the discrete wall temperature

8 distributions. At 1200 LST (Fig. 7(b)), the solar radiation directly heated the ground,

9 and the wall temperatures of leeward and windward surfaces were both symmetric in

10 effect, leading to a lasting symmetric structure of the double-elevated eddies. In contrast,

11 asymmetric wall temperatures were observed on either the leeward or windward

12 surfaces at 0800 and 1600 LST. Thus, similar asymmetric flow structures appeared at

13 0800 and 1600 LST; the northern and southern parts of the Sp-canyon were occupied

14 by the primary circulation and elevated eddies, respectively. This observation is

15 supported by Nazarian and Kleissl [28]. They also revealed that a similar flow structure

16 of a short Sp-canyon could be both found at 0800 and 1600 LST due to the strong

17 influence from the St-canyon, under realistic non-uniform thermal forcing. Notably,

18 this phenomenon could differ from that in some infinite street canyon cases based on

19 the uniform wall heating assumption. Hence, the influences of λ_F on the flow structures

20 were analyzed considering the symmetric (1200 LST) and asymmetric (0800 or 1600

21 LST) wall temperatures.

22 Figure 8 shows the predicted wall temperature contours and 3D streamlines in the

23 Sp-canyon (the orange area at the upper right corner of Fig. 7) for various λ_F values at

24 1200 LST and 1600 LST. Under the symmetric wall temperature (1200 LST), the flow

25 structure remained symmetric elevated eddies as λ_F increased. Under the asymmetric

26 wall temperature (1600 LST), the flow structure first became asymmetric and then

27 became symmetric again as λ_F increased. When λ_F increased to 0.25, the shading effect

28 on the west surface became significant, along with the increasing wall temperature on

1   the north part of the east facade. This strong buoyancy force caused a primary vortex

2   in the northern part of the street canyon. Thus, the airflow structure became asymmetric.

3   When λ_F increased to 1.25, symmetric elevated eddies resulted, since most of the east

4   surface was also subject to the shading effect, and the buoyancy force resulting from

5   the high temperature on the north part of the east surface was not strong enough to

6   generate another primary vortex.

Wall temperature/°C

30 32 34 36 38 40 42 44 46 48

(a) LST= 0800 λ_F=0.25   **(b) LST= 1200 λ_F=0.25**   **(c) LST= 1600 λ_F=0.25**

8   Fig. 7 Predicted wall temperature and 3D streamlines in the Sp-canyon at various solar times for $\lambda_F = 0.25$.
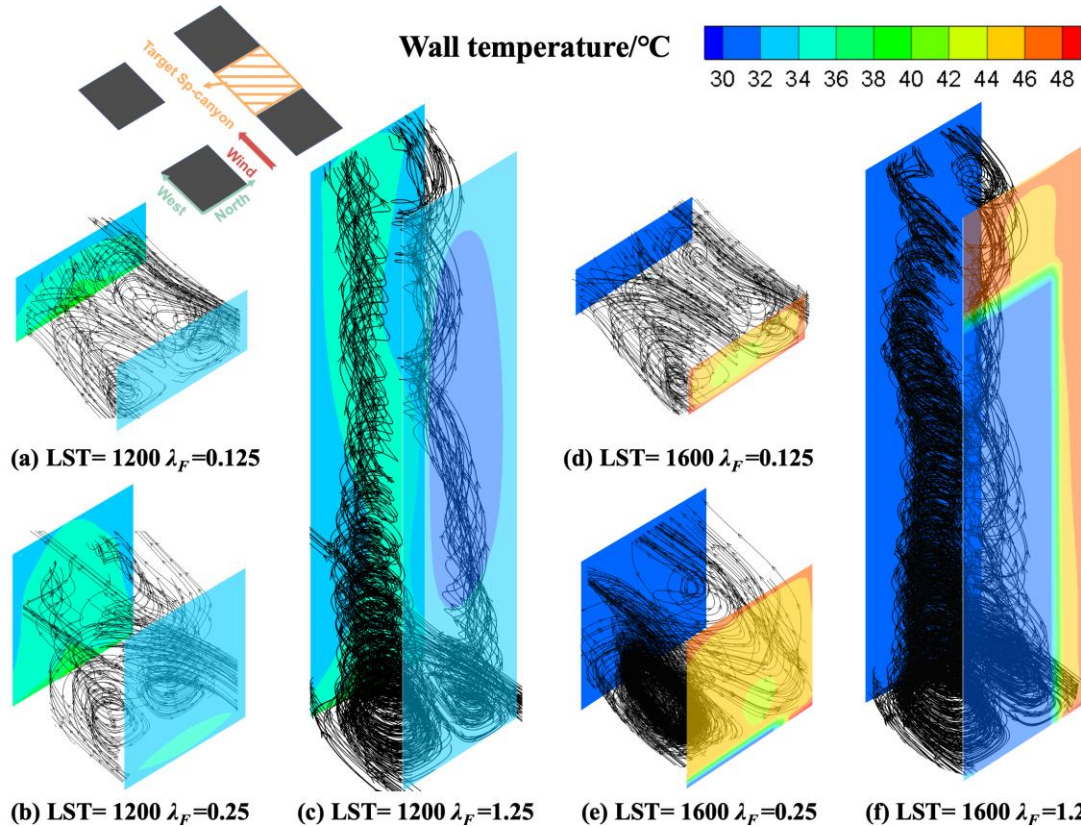
Fig. 8 Predicted wall temperature contours and 3D streamlines in the Sp-canyon for different frontal area densities at 1200 LST and 1600 LST.

Figure 9 shows the predicted wind velocities at the pedestrian level for various λ_F values at 1200 LST and 1600 LST. At 1200 LST, the variant of natural convection was relatively minor, and the wind velocity was strongly related to the forced convection affected by the building structures. Therefore, the wind velocities on the four sidewalks changed slightly when λ_F increased to 0.25. On the other hand, the wind velocities significantly increased due to the significant "venturi effect" when λ_F increased to 1.25. At 1600 LST, the wind velocities on the north or west sidewalks showed similar trends to those at 1200 LST since they were mainly affected by the forced convection of the mainstream. The wind velocity on the south sidewalk decreased substantially when λ_F increased to 0.25 due to the appearance of a wind shadow area affected by the asymmetric flow structure in the Sp-canyon and then rose again when λ_F increased to 1.25. Similarly, the wind velocity on the east sidewalk decreased first and then increased due to the asymmetric flow structure in the Sp-canyon.

24
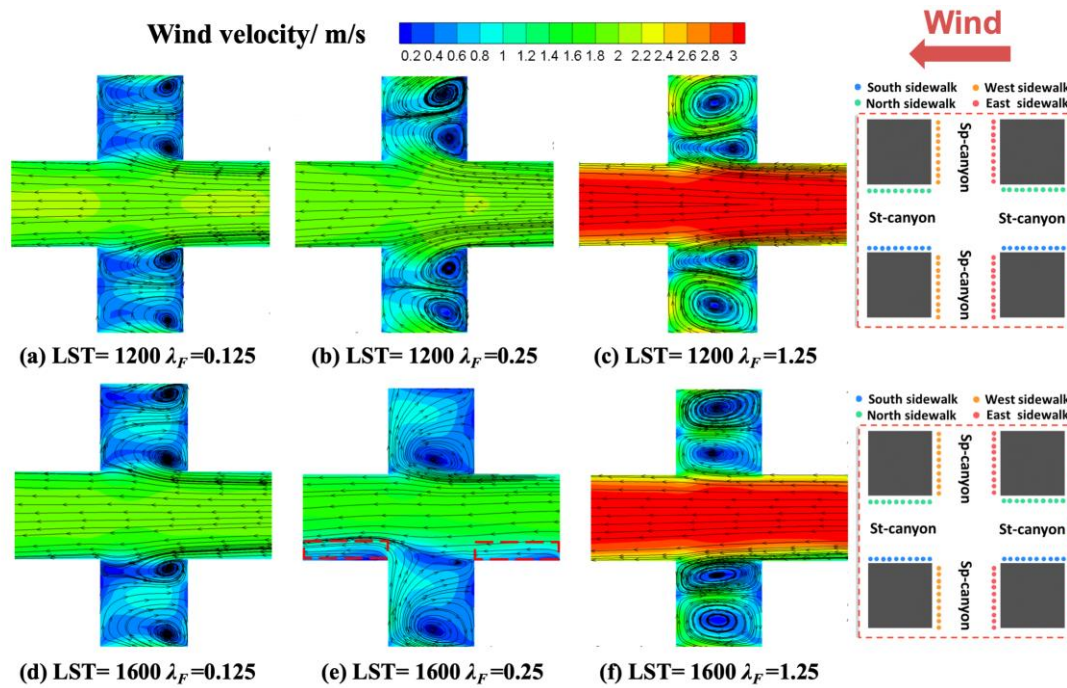
Fig. 9 Predicted wind velocity for different frontal area densities at 1200 LST and 1600 LST (red dashed line denotes the wind shadow area).

Figure 10 summarizes the average wind velocities (over the 10 monitoring points at the pedestrian level) for different λ_F values at 0800 LST, 1200 LST and 1600 LST. The trends at 0800 LST and 1600 LST were very similar and different from those at 1200 LST. At 1200 LST, the average wind velocities on the four sidewalks changed slightly at first until $\lambda_F = 0.25$; then, they escalated considerably (increasing by approximately 1 m/s from $\lambda_F = 0.25$ to 1.25) due to the "venturi effect" of the mainstream. At 0800 LST and 1600 LST, the wind velocity on the west or north sidewalk showed trends similar to those at 1200 LST. The wind velocity on the south sidewalk decreased significantly at first until $\lambda_F = 0.25$ (reducing up to 0.9 m/s from $\lambda_F = 0.15$ to 0.25) due to the wind shadow area, and then it started to increase again rapidly. The wind velocity on the east sidewalk increased slightly at first and then decreased, followed by a gentle increase (approximately 0.3 m/s) when $\lambda_F \geq 0.25$.
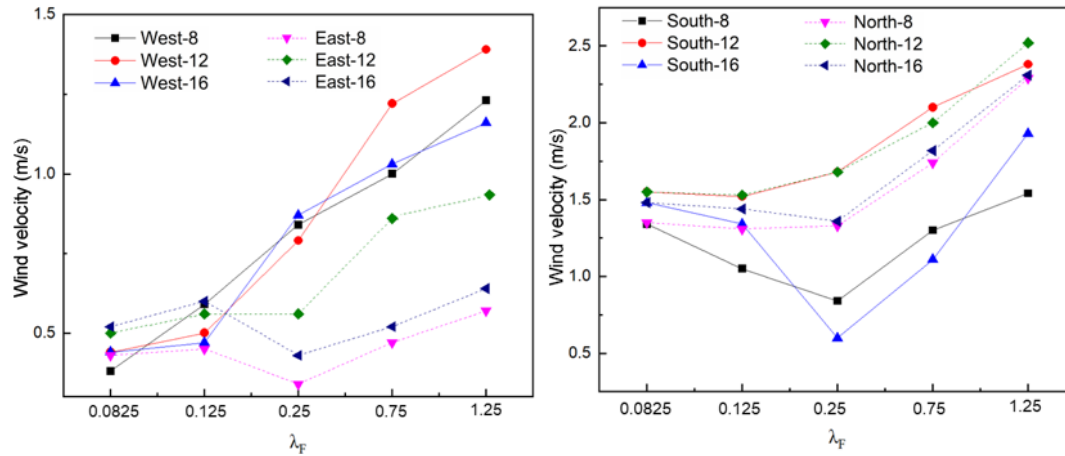
1

2   (a) Sp-canyon   (b) St-canyon

3   Fig. 10 Predicted average wind velocities at the pedestrian level above the sidewalks in the (a) St-canyon and (b)

4   Sp-canyon for different λ_F values at 0800 LST, 1200 LST and 1600 LST.

3.3 Thermal comfort

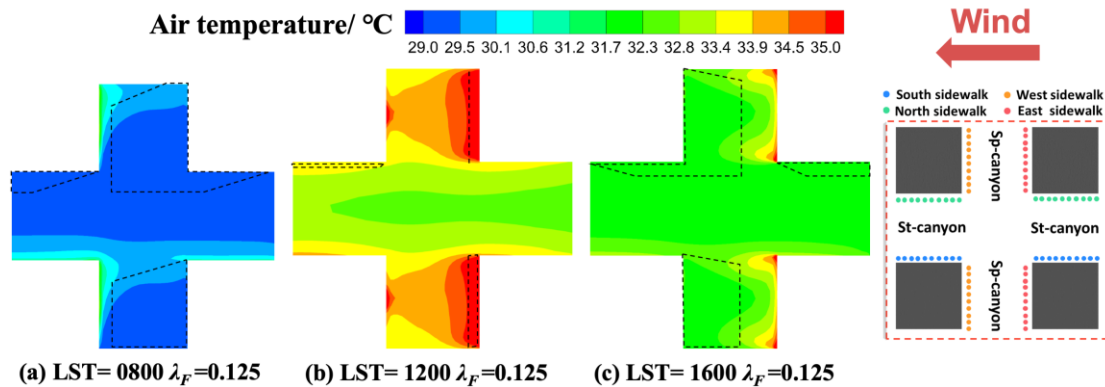**Air Temperature**

7   First, the air temperature at the pedestrian level at various solar times (0800 LST,

8   1200 LST, and 1600 LST) was tested under $\lambda_F = 0.125$. To elucidate the shading effect

9   attributable to different solar positions, the black-dashed frames in Fig. 11 indicate the

10   regions shaded by surrounding buildings at different LSTs. Obviously, the shading

11   effect is the most critical factor in the distribution of the air temperature. Thus, the air

12   temperature at 1200 LST was significantly higher than that at 0800 LST and 1600 LST

13   (2-4 °C higher in the Sp-canyon and 1-3 °C higher in the St-canyon). Meanwhile, the

14   air temperature in the areas exposed to solar radiation (the west side at 0800 LST and

15   the east side at 1600 LST) was 2-3 °C higher than in other regions. Therefore, the

16   influences of λ_F on air temperature were analyzed considering the weak (1200 LST)

17   and strong (1600 LST) shading effects.

18   Figure 12 illustrates the predicted air temperature at the pedestrian level for various

19   λ_F values at 1200 LST and 1600 LST. At 1200 LST, the air temperature on the east and

20   the west sidewalks first increased with λ_F because of the increasingly strong elevated

21   eddies, which are adverse to the dispersion of heat, and then decreased due to the

26

1   enhancement of ventilation and shading. The air temperature on the south sidewalk

2   changed slightly with λ_F because this sidewalk was always exposed to solar radiation.

3   The air temperature on the north sidewalk changed insignificantly with λ_F at first and

4   then decreased by approximately 1 °C due to the increase in shading area. At 1600 LST,

5   the air temperature on the north and west sidewalks remained nearly constant and then

6   decreased by approximately 1-2 °C with increasing λ_F. The possible explanation is that

7   these two sidewalks were always shaded at 1600 LST, and the reduction in air

8   temperature was related to the increase in wind velocity for $\lambda_F = 1.25$. The air

9   temperature on the south sidewalk first increased with λ_F and then decreased as a result

10   of the wind shadow area. The air temperature on the east sidewalk reduced significantly

11   by approximately 3 °C when λ_F increased to 0.25 since the east sidewalk began to be

12   completely shaded (the black-dashed frames started to cover the east sidewalk) (Fig.

13   3(b)); then, it decreased slightly for $\lambda_F = 1.25$.

14   (a) LST= 0800 λ_F=0.125   (b) LST= 1200 λ_F=0.125   (c) LST= 1600 λ_F=0.125

15   Fig. 11 Predicted air temperature contours at the pedestrian level at various solar times when $\lambda_F = 0.125$ (the black-

16   dashed frames indicate the regions shaded by the surrounding buildings).
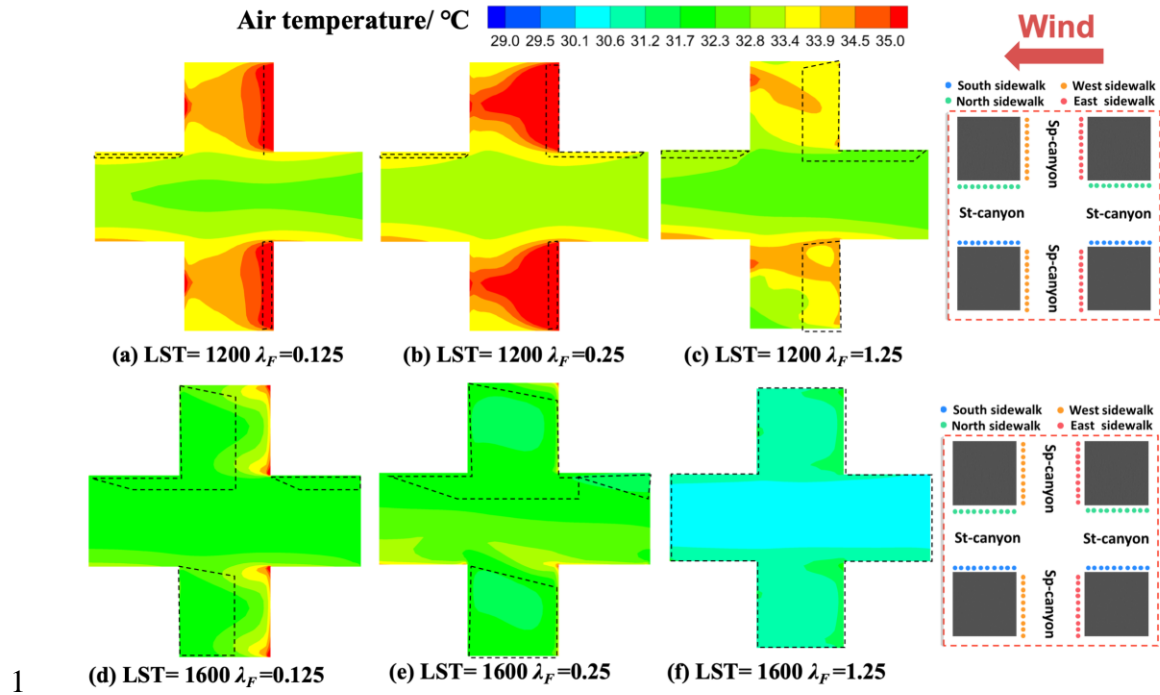
Fig. 12 Predicted air temperature contours at the pedestrian level for various λ_F settings at 1200 LST and 1600 LST

(the black-dashed frames indicate the regions shaded by the surrounding buildings).

Figure 13 summarizes the predicted average air temperature (over the 10 monitoring points at the pedestrian level) for different λ_F values at 0800 LST, 1200 LST and 1600 LST. Generally, the trends at 0800 LST and 1600 LST were again similar and very different from the pattern at 1200 LST. At 1200 LST, the air temperature on the four sidewalks first increased to $\lambda_F = 0.25$ and then decreased or changed only slightly. At 0800 LST or 1600 LST, the air temperature on the west or the east sidewalk decreased gradually with λ_F, especially when λ_F increased to 0.25. The air temperature on the south sidewalk first increased with λ_F and then decreased, but it gradually reduced with λ_F on the north sidewalk.
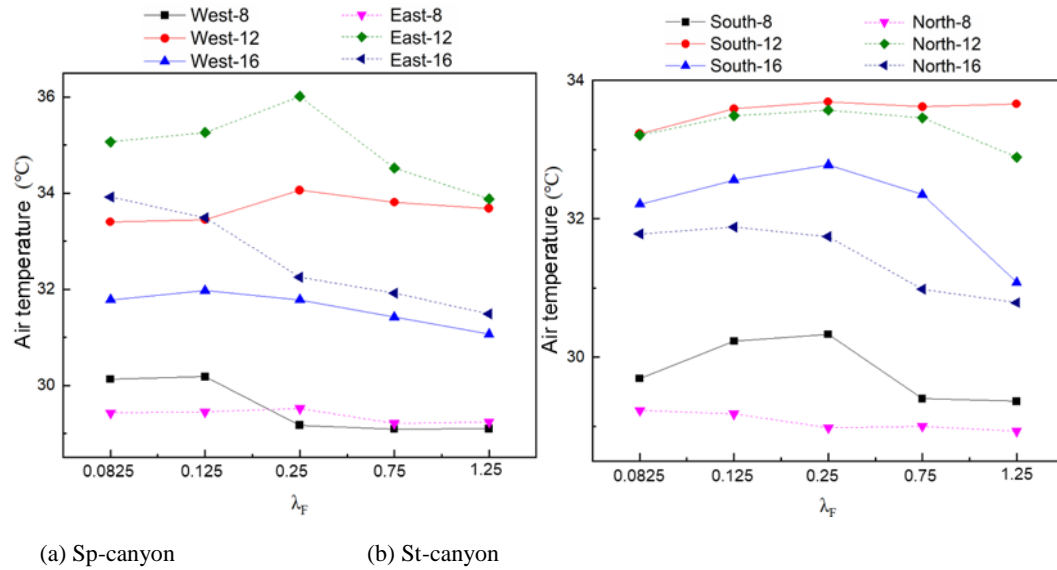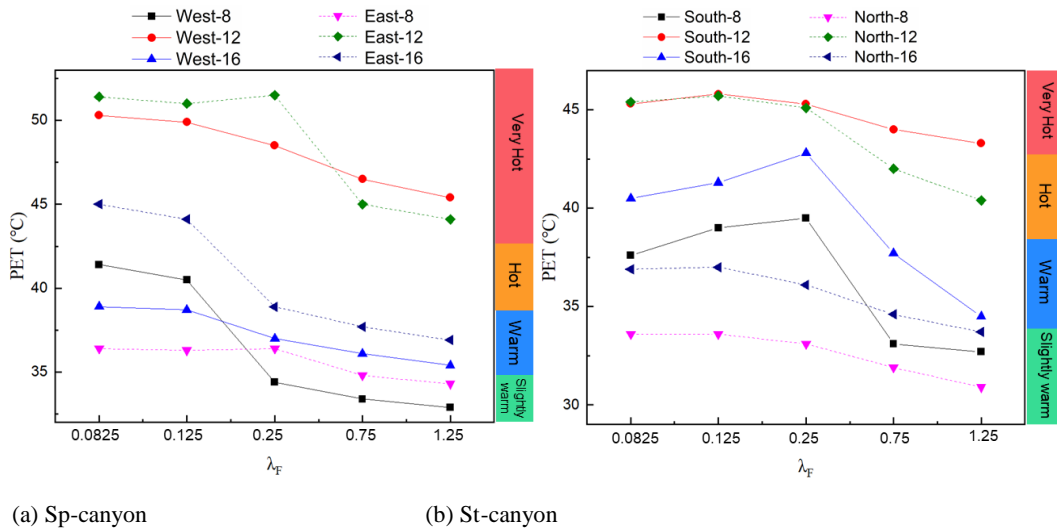
(a) Sp-canyon   (b) St-canyon

Fig. 13 Predicted average air temperatures at the pedestrian level above the sidewalks in the (a) Sp-canyon and (b) St-canyon for different λ_F values at 0800 LST, 1200 LST and 1600 LST.

PET profiles

As shown in Fig. 14, the mean PET development with λ_F at the pedestrian level on the four sidewalks (from 10 monitoring points on each sidewalk, as shown in Fig. 2 (c)) showed the same tendencies as those of the wind velocity and air temperature. The PET at 0800 LST and 1600 LST still showed similar trends, with both being different from that at 1200 LST. For 1200 LST, the PETs on the four sidewalks changed slightly with λ_F, and a sharp decrease (up to 5 °C) occurred in the PET from $\lambda_F = 0.25$ to 0.75, as an apparent increase in the wind velocity lowers the PET, although the air temperature does not decline progressively. Nevertheless, the minimum PET was larger than 40 °C (hot level). For 0800 LST or 1600 LST, the PETs on the east, the west, and the north sidewalks tended to decrease with λ_F, and an evident decrease in the PET from $\lambda_F = 0.125$ to 0.25 occurred for the west sidewalk at 0800 LST and the east sidewalk at 1600, possibly because the increase in λ_F strengthened the wind velocity and the shading effect and thereby caused the decrease in the PET. In addition, the apparent reduction in air temperature led to a significant decrease in the PET (up to 6 °C) when λ_F increased to 0.25 on these three sidewalks. The PET on the south sidewalk escalated at an early stage ($\lambda_F \leq 0.25$) and then obviously declined (up to 7 °C) because of the wind shadow

1 area. In general, the warm level or the slightly warm level could be achieved when λ_F

2 exceeded 0.75 at 0800 LST and 1600 LST.
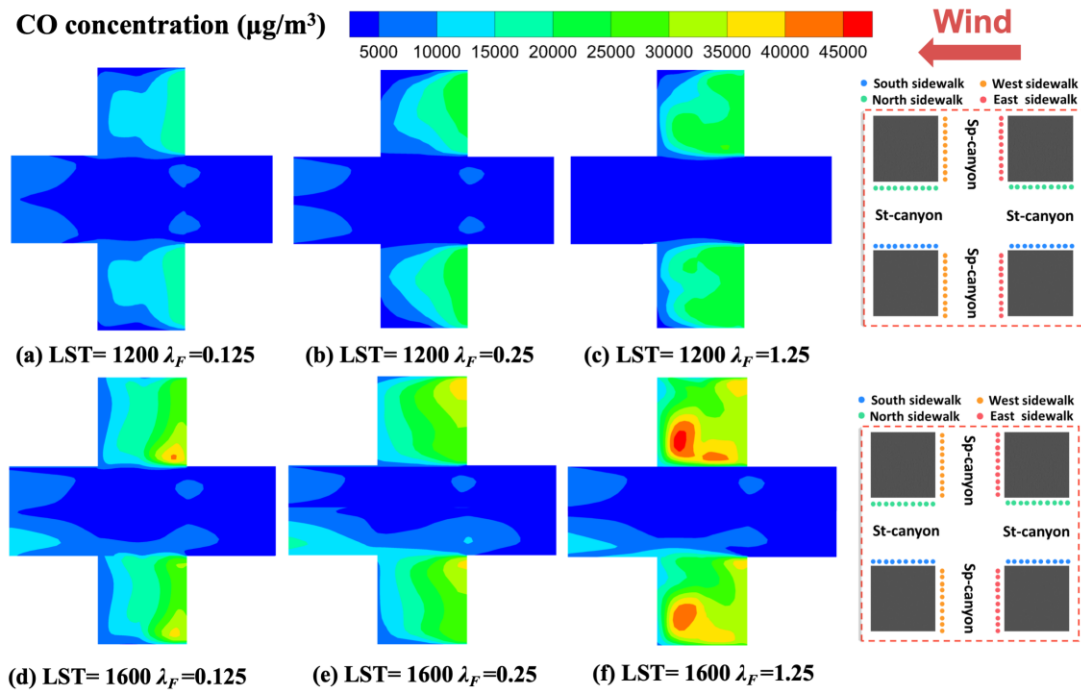

(a) Sp-canyon   (b) St-canyon

Fig. 14 Predicted PET profiles at the pedestrian level above sidewalks in the (a) Sp-canyon and (b) St-canyon for

different λ_F values at 0800 LST, 1200 LST and 1600 LST.

3.4 Air quality

8 Since the distribution of the CO concentration is directly related to the flow

9 structure and wind velocity, the impact of λ_F on the CO concentration is also analyzed

10 considering the symmetric (1200 LST) and asymmetric (0800 or 1600 LST) wall

11 temperature cases. Figure 15 presents the predicted CO concentration contours at the

12 pedestrian level for various λ_F settings at 1200 LST and 1600 LST. At 1200 LST, the

13 CO concentrations on the north and south sidewalks decreased slightly with λ_F and then

14 decreased dramatically due to the noticeable increase in wind velocity at large λ_F. The

15 concentration on the east sidewalk increased gradually with λ_F due to an increase in

16 upward flow resistance and a decrease in buoyancy force. In contrast, the concentration

17 on the west sidewalk changed slightly since the pollutant tended to accumulate on the

18 east side (leeward side). At 1600 LST, the concentrations on the east and west sidewalks

19 increased gradually due to the increase in upward flow resistance caused by the elevated

20 eddies, especially on the east sidewalk. The concentration on the south sidewalk first

1 increased and then decreased due to the wind shadow area. The concentration on the

2 north sidewalk decreased slightly with the increase in λ_F.

(a) LST= 1200 λ_F=0.125   (b) LST= 1200 λ_F=0.25   (c) LST= 1200 λ_F=1.25

(d) LST= 1600 λ_F=0.125   (e) LST= 1600 λ_F=0.25   (f) LST= 1600 λ_F=1.25

4 Fig. 15 Predicted CO concentration contours at the pedestrian level for various λ_F settings at 1200 LST and 1600

5 LST.

6   Figure 16 summarizes the predicted average CO concentration (over the 10

7 monitoring points at the pedestrian level above the four sidewalks) for different λ_F

8 values at 0800 LST, 1200 LST and 1600 LST. Similar trends of the pollutant

9 concentration to those of the λ_F appear at 0800 LST and 1600 LST for each sidewalk.

10 At 1200 LST, the CO concentration on the north or south sidewalks only slightly

11 decreased and then significantly decreased from 4100 μg/m^3 at λ_F = 0.25 to

12 approximately 3000 μg/m^3 at λ_F = 0.75. The CO concentration on the west sidewalk

13 was nearly unchanged. The CO concentration on the east sidewalk increased notably

14 when λ_F increased from 0.125 to 0.25 (from 18000 μg/m^3 at λ_F = 0.125 to 24000 μg/m^3

15 at λ_F = 0.25). For 0800 LST or 1600 LST, the concentration on the east or west

16 sidewalks increased significantly; the concentration on the south sidewalk first

17 increased until λ_F = 0.25 and then decreased; and a slight reduction in the concentration

18 occurred on the north sidewalk.

1
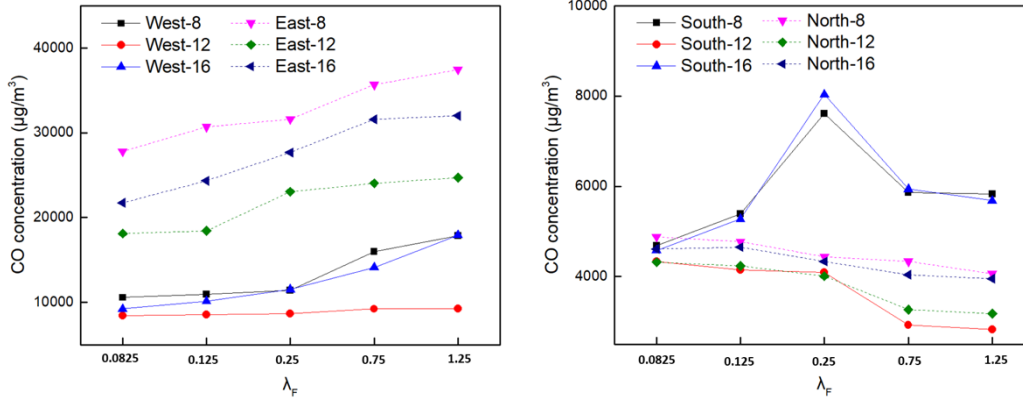
(a) Sp-canyon　　　　　　　　(b) St-canyon

Fig. 16 Predicted average CO concentration profiles at the pedestrian level above the sidewalks: (a) Sp-canyon and

(b) St-canyon for different λ_F values at 0800 LST, 1200 LST and 1600 LST.

3.5 Multivariable regression analyses on thermal comfort and air quality

To achieve better air quality and thermal comfort, the values of both the CO concentration and PET should be small. However, the trends of the average CO concentration at various LSTs on different sidewalks (Fig. 16) were basically opposite that of the average PET (Fig. 14). For example, for the south and north sidewalks, at 1200 LST, the average CO concentrations were lower than those at 0800 LST and 1600 LST (Fig. 16(b)), whereas the average PET at 1200 LST was higher than those at 0800 LST and 1600 LST (Fig. 14(b)). Therefore, the multivariable regression analyses became meaningful because we could evaluate the local thermal comfort and air quality simultaneously based on the regression outcomes.

To generalize and sum up the correlation of the evaluation parameters of interest – normalized CO concentration and PET – with λ_F (from 0.0825 to 1.25) and the LST (0700 to 1700), 8 multivariable regression analyses for the four sidewalks were conducted among a group of dimensionless parameters based on all 50 cases simulated, as shown in Table 3. Herein, the CO concentration (C^*) was normalized by the ambient wind velocity (U_{ref}), reference height (H), and traffic emission rate (Q_c), and the PET was likewise normalized by the ambient air temperature (T_{ref}).

1   According to these 8 correlations, the local PET and CO concentrations for various

2 LSTs and λ_F values could be obtained after inputting the ambient air temperature,

3 ambient wind velocity, reference height, and traffic emission rate. Taking Hong Kong

4 as an example, PET < 38 °C (warm level) and CO concentration < 30000 μg/m^3 (1-hour

5 threshold value of CO set by the Hong Kong Air Quality Objectives) for 70% of the

6 daytime (0700 LST to 1700 LST) on all four sidewalks were introduced as criteria of

7 the frontal area density. For PET < 38 °C in 70% of the daytime, λ_F should be higher

8 than 0.82, 0.52, 0.72, and 0.81 for the north, south, west, and east sidewalks,

9 respectively. For CO concentrations < 30000 μg/m^3 in 70% of the daytime, λ_F should

10 be lower than 1.25, 1.25, 1.25, and 0.84 for the north, south, west, and east sidewalks,

11 respectively. Therefore, the building arrays should have λ_F values less than 0.84 but

12 greater than 0.82 to realize a CO concentration < 30000 μg/m^3 and PET < 38 °C for

13 70% of the daytime.

14   Principally, the correlations obtained with multiple dimensionless parameters can

15 provide a meaningful reference for decision-makers and urban planners in formulating

16 appropriate building density design policies to improve the outdoor thermal comfort

17 and air quality at the pedestrian level.

18   Table 3 Multivariable regression analysis for PET and CO concentration

Index	Sidewalk	Correlation	R^2
PET	East	$\left.\dfrac{PET}{T_{ref}}\right|_E = -1.3 + 0.05\lambda_F + 0.47LST + 0.12\lambda_F{}^2 - 0.018LST^2 - 0.033LST\lambda_F$	0.89
	West	$\left.\dfrac{PET}{T_{ref}}\right|_W = -0.33 - 0.899\lambda_F + 0.37LST + 0.22\lambda_F{}^2 - 0.017LST^2 - 0.03LST\lambda_F$	0.92
	South	$\left.\dfrac{PET}{T_{ref}}\right|_S = -0.34 + 0.05\lambda_F + 0.31LST - 0.04\lambda_F{}^2 - 0.01LST^2 - 0.005LST\lambda_F$	0.89
	North	$\left.\dfrac{PET}{T_{ref}}\right|_N = -1.02 - 0.23\lambda_F + 0.43LST + 0.04\lambda_F{}^2 - 0.017LST^2 - 0.001LST\lambda_F$	0.87
CO concentration	East	$\left.\dfrac{C*U_{ref}*H^2}{Q_C}\right|_E = 1639.08 + 230.07\lambda_F - 289.82LST + 1485.65\lambda_F{}^2 + 12.23LST^2 - -25.91LST\lambda_F$	0.98
	West	$\left.\dfrac{C*U_{ref}*H^2}{Q_C}\right|_W = 1394.52 - 144.52\lambda_F - 240.68LST + 777.76\lambda_F{}^2 + 10.03LST^2 - 4.1LST\lambda_F$	0.97
	South	$\left.\dfrac{C*U_{ref}*H^2}{Q_C}\right|_S = 181.83 + 11.14\lambda_F - 31.57LST + 138.43\lambda_F{}^2 + 1.31LST^2 - 0.8LST\lambda_F$	0.99

| North | $\dfrac{C*U_{ref}*H^2}{Q_C}\Big|_N = 154.2 + 24.86\lambda_F - 27.24 LST + 155.71\lambda_F{}^2 + 1.14 LST^2 - 0.65 LST\lambda_F$ | 0.99 |

4. Limitations

This study attempts to investigate the effects of frontal area density on outdoor thermal comfort and air quality. Some details have been simplified. First, the calculations were conducted only for steady-state weather conditions at specified LSTs to estimate the thermal comfort and air quality of the whole day. Without considering the computational cost, unsteady hourly calculations on these two indices should be conducted to arrive at more comprehensive conclusions. Second, the setting of the ambient wind direction was based on the prevailing wind in June, i.e., the east wind. According to the results above, a similar conclusion could be achieved for the west wind due to the dominant horizontal double-eddy circulation. For some cities whose prevailing wind direction is north or south in summer, the results of the present study may not be applicable. Third, in comparison with the realistic urban model, the generic urban model adopted by this study could provide some convenient but relatively crude estimates for the applications of urban planning [62–64]. Thus, the future work will focus on investigating whether these suggestions from generic building arrays could be successfully applied in some realistic urban canyons to determine their optimal layout.

5. Conclusions

The present study investigated the influence of the frontal area density (λ_F ranges from 0.0825 to 1.25) of 3D building arrays on the thermal comfort and air quality at the pedestrian level above four sidewalks (north, south, east, and west) considering realistic solar irradiation. With the coupling of the ANSYS Fluent® software and the Rayman model, we then obtained the outdoor parameters of the thermal comfort (PET) and air quality (CO concentration). Multivariable regression analyses were conducted to

1 optimize the thermal comfort and air quality conditions. The major results are as
2 follows.

3   (1) With the increase in λ_F, similar trends of the wind velocity, air temperature,
4   PET, and CO concentration are observed at 0800 LST and 1600 LST, all of
5   which differed from those at 1200 LST.

6   (2) With the increase in λ_F, the PET on the four sidewalks decreases gradually, but
7   the values are still higher than the warm level at 1200 LST. A steady reduction
8   in the PET occurs on the east, west, and north sidewalks, but the PET on the
9   south sidewalk increases until $\lambda_F = 0.25$ and then decreases. The PET could
10   achieve a warm level when λ_F exceeds 0.75 at 0800 LST or 1600 LST.

11   (3) With the increase in λ_F, a decrease in the CO concentration occurs on the south
12   and north sidewalks, but the CO concentrations on the east and west sidewalks
13   increase significantly and change slightly, respectively, at 1200 LST; the
14   maximum concentration is lower than 30000 $\mu g/m^3$ at 1200 LST. At 0800 LST
15   or 1600 LST, the concentration first increases and then decreases on the south
16   sidewalk; the maximum concentration is approximately 8000 $\mu g/m^3$. The
17   concentration on the east or the west sidewalk increases gradually and can
18   exceed 30000 $\mu g/m^3$ when $\lambda_F > 0.25$.

19   (4) The elevated eddy is adverse to the updating of air, in contrast to the primary
20   circulation. The elevated eddy in-between the buildings should, therefore, be
21   minimized to improve the AQ.

22   (5) Two multivariable regression analyses for all of the simulated cases were
23   conducted. Two dimensionless parameters of the CO concentration and PET
24   were correlated with the LST and λ_F separately. These correlations provide a
25   reference for the design of urban density, which will improve the thermal
26   comfort and air quality simultaneously. In Hong Kong, the building arrays
27   should have λ_F values less than 0.84 but greater than 0.82 to realize a CO
28   concentration < 30000 $\mu g/m^3$ and PET < 38 °C for 70% of the daytime in June.

5.1 Suggestions for urban planners

Based on the present study, the following suggestions are proposed for better thermal comfort and air quality in a dense, hot-humid city:

1) Although the wind velocity at the pedestrian level is affected to some extent by the buoyancy force, it is mainly relevant to building configurations and city densities. Therefore, previous studies or strategies for improving the wind velocity without consideration of the thermal effect could still apply.

2) Three main factors affect the PET at the pedestrian level: shading effect, air temperature, and wind velocity. Increasing the building height is a significant method for enhancing the shading effect, improving ventilation, and reducing the air temperature to lower the PET further.

3) The street orientation, which could directly affect the solar radiation distribution in urban areas, has a critical effect on the outdoor thermal comfort and pollution distribution. Thus, urban designers should formulate specific optimization strategies for different street orientations or various sidewalks.

Reference:

[1] A. Haines, R.S. Kovats, D. Campbell-Lendrum, C. Corvalan, Climate change and human health: Impacts, vulnerability and public health, Public Health. 120 (2006) 585–596. https://doi.org/https://doi.org/10.1016/j.puhe.2006.01.002.

[2] Y. Yu, J. Liu, K. Chauhan, R. de Dear, J. Niu, Experimental study on convective heat transfer coefficients for the human body exposed to turbulent wind conditions, Build. Environ. 169 (2020) 106533. https://doi.org/https://doi.org/10.1016/j.buildenv.2019.106533.

[3] Y. Xiong, J. Liu, J. Kim, Understanding differences in thermal comfort between urban and rural residents in hot summer and cold winter climate, Build. Environ. 165 (2019) 106393. https://doi.org/https://doi.org/10.1016/j.buildenv.2019.106393.

[4] C. Cai, T. Ming, W. Fang, R. de Richter, C. Peng, The effect of turbulence induced by different kinds of moving vehicles in street canyons, Sustain. Cities Soc. 54 (2020) 102015. https://doi.org/10.1016/J.SCS.2020.102015.

[5] Z. Luo, Y. Li, W.W. Nazaroff, Intake fraction of nonreactive motor vehicle exhaust in Hong Kong, Atmos. Environ. 44 (2010) 1913–1918. https://doi.org/https://doi.org/10.1016/j.atmosenv.2010.02.016.

[6]   W.-Y. Ng, C.-K. Chau, A modeling investigation of the impact of street and building configurations on personal air pollutant exposure in isolated deep urban canyons, Sci. Total Environ. 468–469 (2014) 429–448. https://doi.org/https://doi.org/10.1016/j.scitotenv.2013.08.077.

[7]   Y. Du, C.M. Mak, Z. Ai, Modelling of pedestrian level wind environment on a high-quality mesh: A case study for the HKPolyU campus, Environ. Model. Softw. 103 (2018) 105–119. https://doi.org/https://doi.org/10.1016/j.envsoft.2018.02.016.

[8]   Y. Du, B. Blocken, S. Pirker, A novel approach to simulate pollutant dispersion in the built environment: Transport-based recurrence CFD, Build. Environ. 170 (2020) 106604. https://doi.org/https://doi.org/10.1016/j.buildenv.2019.106604.

[9]   D. Cui, X. Li, Y. Du, C.M. Mak, K. Kwok, Effects of envelope features on wind flow and pollutant exposure in street canyons, Build. Environ. 176 (2020) 106862. https://doi.org/https://doi.org/10.1016/j.buildenv.2020.106862.

[10]   J. Hang, X. Chen, G. Chen, T. Chen, Y. Lin, Z. Luo, X. Zhang, Q. Wang, The influence of aspect ratios and wall heating conditions on flow and passive pollutant exposure in 2D typical street canyons, Build. Environ. (2019) 106536. https://doi.org/https://doi.org/10.1016/j.buildenv.2019.106536.

[11]   K. Zhang, G. Chen, Y. Zhang, S. Liu, X. Wang, B. Wang, J. Hang, Integrated impacts of turbulent mixing and NOX-O3 photochemistry on reactive pollutant dispersion and intake fraction in shallow and deep street canyons, Sci. Total Environ. 712 (2020) 135553. https://doi.org/https://doi.org/10.1016/j.scitotenv.2019.135553.

[12]   A. Mochida, I.Y.F. Lun, Prediction of wind environment and thermal comfort at pedestrian level in urban area, J. Wind Eng. Ind. Aerodyn. 96 (2008) 1498–1527. https://doi.org/https://doi.org/10.1016/j.jweia.2008.02.033.

[13]   X. Xie, C.-H. Liu, D.Y.C. Leung, Impact of building facades and ground heating on wind flow and pollutant transport in street canyons, Atmos. Environ. 41 (2007) 9030–9049. https://doi.org/https://doi.org/10.1016/j.atmosenv.2007.08.027.

[14]   R. Ramponi, B. Blocken, L.B. de Coo, W.D. Janssen, CFD simulation of outdoor ventilation of generic urban configurations with different urban densities and equal and unequal street widths, Build. Environ. 92 (2015) 152–166. https://doi.org/https://doi.org/10.1016/j.buildenv.2015.04.018.

[15]   S.-J. Mei, C.-W. Liu, D. Liu, F.-Y. Zhao, H.-Q. Wang, X.-H. Li, Fluid mechanical dispersion of airborne pollutants inside urban street canyons subjecting to multi-component ventilation and unstable thermal stratifications, Sci. Total Environ. 565 (2016) 1102–1115. https://doi.org/https://doi.org/10.1016/j.scitotenv.2016.05.150.

[16]   L. Lin, J. Hang, X. Wang, X. Wang, S. Fan, Q. Fan, Y. Liu, Integrated Effects of Street Layouts and Wall Heating on Vehicular Pollutant Dispersion and their Reentry Toward Downstream Canyons, Aerosol Air Qual. Res. 16 (2016) 3142–3163. https://doi.org/10.4209/aaqr.2016.04.0148.

[17]   S. Sun, X. Xu, Z. Lao, W. Liu, Z. Li, E.H. García, L. He, J. Zhu, Evaluating the impact of urban green space and landscape design parameters on thermal comfort in hot summer by numerical simulation, Build. Environ. 123 (2017) 277–288. https://doi.org/https://doi.org/10.1016/j.buildenv.2017.07.010.

[18]   J. Hang, Y. Li, M. Sandberg, R. Buccolieri, S. Di Sabatino, The influence of building height variability on pollutant dispersion and pedestrian ventilation in idealized high-rise urban areas, Build. Environ. 56 (2012) 346–360. https://doi.org/https://doi.org/10.1016/j.buildenv.2012.03.023.

[19] R. Buccolieri, M. Sandberg, S. Di Sabatino, City breathability and its link to pollutant concentration distribution within urban-like geometries, Atmos. Environ. 44 (2010) 1894–1903. https://doi.org/https://doi.org/10.1016/j.atmosenv.2010.02.022.

[20] S.-J. Mei, J.-T. Hu, D. Liu, F.-Y. Zhao, Y. Li, H.-Q. Wang, Airborne pollutant dilution inside the deep street canyons subjecting to thermal buoyancy driven flows: Effects of representative urban skylines, Build. Environ. 149 (2019) 592–606. https://doi.org/https://doi.org/10.1016/j.buildenv.2018.12.050.

[21] J. Liu, J. Niu, Q. Xia, Combining measured thermal parameters and simulated wind velocity to predict outdoor thermal comfort, Build. Environ. 105 (2016) 185–197. https://doi.org/https://doi.org/10.1016/j.buildenv.2016.05.038.

[22] X. Xie, C.-H. Liu, D.Y.C. Leung, M.K.H. Leung, Characteristics of air exchange in a street canyon with ground heating, Atmos. Environ. 40 (2006) 6396–6409. https://doi.org/https://doi.org/10.1016/j.atmosenv.2006.05.050.

[23] Z. Tan, J. Dong, Y. Xiao, J. Tu, A numerical study of diurnally varying surface temperature on flow patterns and pollutant dispersion in street canyons, Atmos. Environ. 104 (2015) 217–227. https://doi.org/https://doi.org/10.1016/j.atmosenv.2015.01.027.

[24] W. Zhang, C.M. Mak, Z.T. Ai, W.M. Siu, A Study of the Ventilation and Thermal Comfort of the Environment Surrounding a New University Building under Construction, Indoor Built Environ. 21 (2012) 568–582. https://doi.org/10.1177/1420326X11419871.

[25] N. Nazarian, J. Fan, T. Sin, L. Norford, J. Kleissl, Predicting outdoor thermal comfort in urban environments: A 3D numerical model for standard effective temperature, Urban Clim. 20 (2017) 251–267. https://doi.org/https://doi.org/10.1016/j.uclim.2017.04.011.

[26] W. Wang, E. Ng, Air ventilation assessment under unstable atmospheric stratification — A comparative study for Hong Kong, Build. Environ. 130 (2018) 1–13. https://doi.org/https://doi.org/10.1016/j.buildenv.2017.12.018.

[27] J.L. Santiago, E.S. Krayenhoff, A. Martilli, Flow simulations for simplified urban configurations with microscale distributions of surface thermal forcing, Urban Clim. 9 (2014) 115–133. https://doi.org/https://doi.org/10.1016/j.uclim.2014.07.008.

[28] N. Nazarian, J. Kleissl, Realistic solar heating in urban areas: Air exchange and street-canyon ventilation, Build. Environ. 95 (2016) 75–93. https://doi.org/https://doi.org/10.1016/j.buildenv.2015.08.021.

[29] Y. Qu, M. Milliez, L. Musson-Genon, B. Carissimo, Numerical study of the thermal effects of buildings on low-speed airflow taking into account 3D atmospheric radiation in urban canopy, J. Wind Eng. Ind. Aerodyn. 104–106 (2012) 474–483. https://doi.org/https://doi.org/10.1016/j.jweia.2012.03.008.

[30] M. Taleghani, U. Berardi, The effect of pavement characteristics on pedestrians' thermal comfort in Toronto, Urban Clim. 24 (2018) 449–459. https://doi.org/https://doi.org/10.1016/j.uclim.2017.05.007.

[31] A.-S. Yang, Y.-H. Juan, C.-Y. Wen, C.-J. Chang, Numerical simulation of cooling effect of vegetation enhancement in a subtropical urban park, Appl. Energy. 192 (2017) 178–200. https://doi.org/https://doi.org/10.1016/j.apenergy.2017.01.079.

[32] J. Srebric, M. Heidarinejad, J. Liu, Building neighborhood emerging properties and their impacts on multi-scale modeling of building energy and airflows, Build. Environ. 91 (2015) 246–262. https://doi.org/https://doi.org/10.1016/j.buildenv.2015.02.031.

[33]   E. Ng, C. Yuan, L. Chen, C. Ren, J.C.H. Fung, Improving the wind environment in high-density cities by understanding urban morphology and surface roughness: A study in Hong Kong, Landsc. Urban Plan. 101 (2011) 59–74. https://doi.org/https://doi.org/10.1016/j.landurbplan.2011.01.004.

[34]   J. Hang, Y. Li, Age of air and air exchange efficiency in high-rise urban areas and its link to pollutant dilution, Atmos. Environ. 45 (2011) 5572–5585. https://doi.org/https://doi.org/10.1016/j.atmosenv.2011.04.051.

[35]   G. Chen, L. Rong, G. Zhang, Comparison of urban airflow between solar-induced thermal wall and uniform wall temperature boundary conditions by coupling CitySim and CFD, Build. Environ. 172 (2020) 106732. https://doi.org/https://doi.org/10.1016/j.buildenv.2020.106732.

[36]   Y.-H. Juan, A.-S. Yang, C.-Y. Wen, Y.-T. Lee, P.-C. Wang, Optimization procedures for enhancement of city breathability using arcade design in a realistic high-rise urban area, Build. Environ. 121 (2017) 247–261. https://doi.org/https://doi.org/10.1016/j.buildenv.2017.05.035.

[37]   S. Bottillo, A.D.L. Vollaro, G. Galli, A. Vallati, Fluid dynamic and heat transfer parameters in an urban canyon, Sol. Energy. 99 (2014) 1–10. https://doi.org/https://doi.org/10.1016/j.solener.2013.10.031.

[38]   H. Yang, T. Chen, Y. Lin, R. Buccolieri, M. Mattsson, M. Zhang, J. Hang, Q. Wang, Integrated impacts of tree planting and street aspect ratios on CO dispersion and personal exposure in full-scale street canyons, Build. Environ. 169 (2020) 106529. https://doi.org/https://doi.org/10.1016/j.buildenv.2019.106529.

[39]   J. Hang, Z. Xian, D. Wang, C.M. Mak, B. Wang, Y. Fan, The impacts of viaduct settings and street aspect ratios on personal intake fraction in three-dimensional urban-like geometries, Build. Environ. 143 (2018) 138–162. https://doi.org/https://doi.org/10.1016/j.buildenv.2018.07.001.

[40]   K. Giannopoulou, M. Santamouris, I. Livada, C. Georgakis, Y. Caouris, The Impact of Canyon Geometry on Intra Urban and Urban: Suburban Night Temperature Differences Under Warm Weather Conditions, Pure Appl. Geophys. 167 (2010) 1433–1449. https://doi.org/10.1007/s00024-010-0099-8.

[41]   Y. Tominaga, A. Mochida, R. Yoshie, H. Kataoka, T. Nozu, M. Yoshikawa, T. Shirasawa, AIJ guidelines for practical applications of CFD to pedestrian wind environment around buildings, J. Wind Eng. Ind. Aerodyn. 96 (2008) 1749–1761. https://doi.org/https://doi.org/10.1016/j.jweia.2008.02.058.

[42]   HKO (Hong Kong Observatory), Statistical data of weather information in Hong Kong;, (2019).

[43]   D.M. Hargreaves, N.G. Wright, On the use of the k–ε model in commercial CFD software to model the neutral atmospheric boundary layer, J. Wind Eng. Ind. Aerodyn. 95 (2007) 355–369. https://doi.org/https://doi.org/10.1016/j.jweia.2006.08.002.

[44]   S. Dugaria, M. Bortolato, D. Del Col, Modelling of a direct absorption solar receiver using carbon based nanofluids under concentrated solar radiation, Renew. Energy. 128 (2018) 495–508. https://doi.org/https://doi.org/10.1016/j.renene.2017.06.029.

[45]   Y. Tominaga, T. Stathopoulos, Turbulent Schmidt numbers for CFD analysis with various types of flowfield, Atmos. Environ. 41 (2007) 8091–8099. https://doi.org/https://doi.org/10.1016/j.atmosenv.2007.06.054.

[46]   V. Yakhot, S.A. Orszag, Renormalization group analysis of turbulence. I. Basic theory, J. Sci. Comput. 1 (1986) 3–51. https://doi.org/10.1007/BF01061452.

[47]   K. An, S.-M. Wong, J.C.-H. Fung, E. Ng, Revisit of prevailing practice guidelines and investigation of topographical treatment techniques in CFD-Based air ventilation assessments, Build. Environ. 169 (2020) 106580. https://doi.org/https://doi.org/10.1016/j.buildenv.2019.106580.

[48] A. Matzarakis, F. Rutz, H. Mayer, Modelling radiation fluxes in simple and complex environments--- application of the RayMan model, Int. J. Biometeorol. 51 (2007) 323–334. https://doi.org/10.1007/s00484-006-0061-8.

[49] K.-M. Wai, E.Y.Y. Ng, C.M.S. Wong, T.Z. Tan, T.-H. Lin, W.-H. Lien, P.A. Tanner, C.S.H. Wang, K.K.L. Lau, N.M.H. He, J. Kim, Aerosol pollution and its potential impacts on outdoor human thermal sensation: East Asian perspectives, Environ. Res. 158 (2017) 753–758. https://doi.org/https://doi.org/10.1016/j.envres.2017.07.036.

[50] Y.-C. Chen, T.-P. Lin, A. Matzarakis, Comparison of mean radiant temperature from field experiment and modelling: a case study in Freiburg, Germany, Theor. Appl. Climatol. 118 (2014) 535–551. https://doi.org/10.1007/s00704-013-1081-z.

[51] K.-M. Wai, C. Yuan, A. Lai, P.K.N. Yu, Relationship between pedestrian-level outdoor thermal comfort and building morphology in a high-density city, Sci. Total Environ. 708 (2020) 134516. https://doi.org/https://doi.org/10.1016/j.scitotenv.2019.134516.

[52] D. Liu, S. Hu, J. Liu, Contrasting the performance capabilities of urban radiation field between three microclimate simulation tools, Build. Environ. 175 (2020) 106789. https://doi.org/https://doi.org/10.1016/j.buildenv.2020.106789.

[53] D. Fröhlich, M. Gangwisch, A. Matzarakis, Effect of radiation and wind on thermal comfort in urban environments - Application of the RayMan and SkyHelios model, Urban Clim. 27 (2019) 1–7. https://doi.org/10.1016/j.uclim.2018.10.006.

[54] T.-P. Lin, Thermal perception, adaptation and attendance in a public square in hot and humid regions, Build. Environ. 44 (2009) 2017–2026. https://doi.org/https://doi.org/10.1016/j.buildenv.2009.02.004.

[55] H. Mayer, P. Höppe, Thermal comfort of man in different urban environments, Theor. Appl. Climatol. 38 (1987) 43–49. https://doi.org/10.1007/BF00866252.

[56] P. Höppe, The physiological equivalent temperature -- a universal index for the biometeorological assessment of the thermal environment, Int. J. Biometeorol. 43 (1999) 71–75. https://doi.org/10.1007/s004840050118.

[57] Y. Xie, T. Huang, J. Li, J. Liu, J. Niu, C.M. Mak, Z. Lin, Evaluation of a multi-nodal thermal regulation model for assessment of outdoor thermal comfort: Sensitivity to wind speed and solar radiation, Build. Environ. 132 (2018) 45–56. https://doi.org/https://doi.org/10.1016/j.buildenv.2018.01.025.

[58] A. Matzarakis, H. Mayer, M.G. Iziomon, Applications of a universal thermal index: physiological equivalent temperature, Int. J. Biometeorol. 43 (1999) 76–84. https://doi.org/10.1007/s004840050119.

[59] T.-P. Lin, A. Matzarakis, Tourism climate and thermal comfort in Sun Moon Lake, Taiwan, Int. J. Biometeorol. 52 (2008) 281–290. https://doi.org/10.1007/s00484-007-0122-7.

[60] K. Uehara, S. Murakami, S. Oikawa, S. Wakamatsu, Wind tunnel experiments on how thermal stratification affects flow in and above urban street canyons, Atmos. Environ. 34 (2000) 1553–1562. https://doi.org/https://doi.org/10.1016/S1352-2310(99)00410-0.

[61] R.N. Meroney, M. Pavageau, S. Rafailidis, M. Schatzmann, Study of line source characteristics for 2-D physical modelling of pollutant dispersion in street canyons, J. Wind Eng. Ind. Aerodyn. 62 (1996) 37–56. https://doi.org/https://doi.org/10.1016/S0167-6105(96)00057-8.

[62] Y. Du, C.M. Mak, Improving pedestrian level low wind velocity environment in high-density cities: A general framework and case study, Sustain. Cities Soc. 42 (2018) 314–324. https://doi.org/https://doi.org/10.1016/j.scs.2018.08.001.

[63]   Y. Du, C.M. Mak, T. Huang, J. Niu, Towards an integrated method to assess effects of lift-up design on outdoor thermal comfort in Hong Kong, Build. Environ. 125 (2017) 261–272. https://doi.org/https://doi.org/10.1016/j.buildenv.2017.09.001.

[64]   Y. Du, C.M. Mak, Y. Li, A multi-stage optimization of pedestrian level wind environment and thermal comfort with lift-up design in ideal urban canyons, Sustain. Cities Soc. 46 (2019) 101424. https://doi.org/https://doi.org/10.1016/j.scs.2019.101424.

[65]   D.K. Fidaros, C.A. Baxevanou, T. Bartzanas, C. Kittas, Numerical simulation of thermal behavior of a ventilated arc greenhouse during a solar day, Renew. Energy. 35 (2010) 1380–1386. https://doi.org/https://doi.org/10.1016/j.renene.2009.11.013.

Table A.1 Mean hourly air temperatures in June in Hong Kong

LST	07 00	08 00	09 00	10 00	11 00	12 00	13 00	14 00	15 00	16 00	17 00
Air temperature	27	27.3	27.7	28.1	28.5	28.8	29	29.1	29.1	29.1	28.8

Table A.2 Spectral optical and thermos-physical material properties[65]

Property	Fluid	Building	Ground
Materials	Air	Concrete	Asphalt
Density (kg/m^3)	1.225	2400	2360
Specific heat (J/kg K)	1006.43	750	920
Thermal conductivity (W/m K)	0.0242	1.7	0.75
Viscosity (kg/m S)	1.7894×10^5	-	-
Absorption coefficient (1/m)	0.19	0.9	0.9
Scattering coefficient (1/m)	0	0	-10
Refractive index	1	1.7	1.92
Emissivity, ε	0.9	0.7	0.95

Table A.3 Classification of thermal sensation [59]

Thermal	PET range (℃)	Thermal	PET range (℃)
Very Cold	<14	Slightly warm	30–34
Cold	14–18	Warm	34–38
Cool	18–22	Hot	38–42
Slightly cool	22–26	Very hot	<42
Neutral	26–30		